International Journal of Mechanical Sciences 217 (2022) 106983

Contents lists available at ScienceDirect

International Journal of Mechanical Sciences

journal homepage: www.elsevier.com/locate/ijmecsci

Improving the performance of a two-sided vibro-impact energy harvester with asymmetric restitution coefficients

Sam Dulin [a], Kailee Lin [b], Larissa Serdukova [c,*], Rachel Kuske [d], Daniil Yurchenko [e]

[a] Department of Mathematics, University of Virginia, USA
[b] Department of Mathematics, Harvey Mudd College, USA
[c] Department of Mathematics and Statistics, University of Reading, Reading, RG6 6AX, UK
[d] School of Mathematics, Georgia Institute of Technology, Atlanta, GA 30313, USA
[e] IMPEE, Heriot-Watt University, Edinburgh, EH14 4AS, UK

ARTICLE INFO

Keywords:
Energy harvesting
Vibro-impact system
Output voltage
Grazing bifurcation
Periodic solutions
Non-smooth dynamics

ABSTRACT

We study the influence of asymmetric restitution coefficients in a model of a two-sided vibro-impact energy harvester (VI-EH), considering the dynamical behavior and the implications for energy output. In the VI-EH, a ball moves freely within a forced cylinder and collides with a compliant dielectric polymer on either end, thus converting the motion into output voltage. We develop (semi-)analytical results for 1:1 periodic solutions, with alternating impacts on either end, focusing on the case of asymmetric restitution coefficients on the top and bottom of the cylinder. New types of 1:1 periodic solutions are found, with energy output clearly different from the symmetric setting. The analysis covers non-intuitive results, including the non-monotonic dependencies of the energy output on the asymmetric restitution coefficients. We find unexpected parameter ranges with improved levels of energy output, as well as stability results indicating that this output is robust to parameter fluctuations or external perturbations. Furthermore, by identifying parameter combinations that limit performance through asymmetries, we show how asymmetric restitution coefficients can counteract these detrimental effects. The analysis is based on maps for the dynamics between impacts, leading to a series of conditions for stable 1:1 periodic solutions in terms of the system parameters. We compare stability and bifurcation structure obtained analytically and numerically. The analysis shows possible regions of bi-stability between different behaviors that may not be captured by numerical approaches.

1. Introduction

Energy Harvesting (EH) refers to a process of generating electrical power from various renewable energy sources such as wind, waves, and tides. More often, however, EH is used in a narrower sense and referred to energy scavenging from natural and man-made vibrations. A number of approaches have been proposed to convert mechanical energy of vibrations into electrical output, including piezoelectric [1], electromagnetic [2], electrostatic [3,4] and triboelectric [5,6]. To absorb available energy effectively, various mechanical systems have been developed, depending on their specific applications. In the beginning of this century the linear single and multi-degree of freedom systems, as well as continuous systems like nano-, micro- and macro-scale beams, have been proposed to serve as energy scavengers. Theoretical foundations of energy harvesting, developed for such electro-mechanical devices in the last twenty years, have been well supported by numerical simulations and experimental findings for deterministic or stochastic excitations [7,8]. It quickly became clear that linear systems were insufficient for generating a reasonable amount of power under excitations with varying frequencies. Moreover, the desired high power output can be achieved only near resonance, leading to reliability and fatigue issues [9,10].

Due to these limitations, scientists have shifted the research focus to linear parametrically excited and nonlinear energy harvesting systems. For example, the response of a parametrically excited spring–mass system is amplified when operating near stability boundaries [11–17], whereas the response of a parametrically excited pendulum becomes rotational [18–20]. Often a nonlinearity is introduced into the system to improve its performance and amplify its response. Furthermore, multi-stable equilibria systems have become very popular in various applications due to high energy harvesting efficiency [21–24]. In other

* Corresponding author.
E-mail addresses: swd7tw@virginia.edu (S. Dulin), klin52@jhu.edu (K. Lin), l.i.serdukova@reading.ac.uk (L. Serdukova), rachel@math.gatech.edu (R. Kuske), d.yurchenko@hw.ac.uk (D. Yurchenko).

https://doi.org/10.1016/j.ijmecsci.2021.106983
Received 6 August 2021; Received in revised form 23 November 2021; Accepted 2 December 2021
Available online 28 December 2021

applications, such as in flow-induced vibrations, the nonlinearity is naturally present in the system [25,26]. Another class of nonlinear systems consists of piecewise-linear and strongly nonlinear vibro-impact (VI) systems. A piecewise-linear system typically comprises a combination of linear springs, where any additional spring is located at a given distance from the system's equilibrium and is engaged only when the mass crosses the predefined distance. Varying this distance can broaden the system's bandwidth and facilitate its tuning to particular environmental conditions [27–29]. VI systems have also been proposed for energy harvesting, but in the vast majority of cases the impacts were introduced to create more favorable dynamics or widen the system's bandwidth, rather than using the impacts as a direct source of energy extraction. A collection of pre-2017 VI energy harvesting concepts were reported in [30]. Since then some new concepts utilizing the benefits of VI dynamic behavior have been proposed in [6,31–33].

VI systems generate a range of rich and diverse nonlinear phenomena, including a variety of bifurcations, sticking, grazing, and chaos [34–36]. A typical VI system consists of a mass impacting against another mass, organizing a VI-pair, or a rigid barrier, where the velocities before and after impact are connected by a restitution coefficient $0 < r \leq 1$. When the system's dominant energy losses come from the impacts, while neglecting other types of damping, the system is conservative between the impacts, maintaining its constant energy level. This creates a valuable opportunity for studying the system via a (semi-)analytical approach, based on maps that combine the dynamics between impacts with the impact conditions. A number of classical references take this approach to study the dynamics, bifurcation and stability of a periodic motion, as well as the grazing phenomenon in vibro-impact systems [37–45]. In general the derived maps cannot be solved explicitly, and have to be treated semi-analytically or numerically. Nevertheless, this approach facilitates the exploration of various periodic solutions, their bifurcations and instabilities.

Recently, a pioneering device in vibro-impact energy harvesting (VI-EH) systems has been proposed in which two dielectric elastomeric (DE) membranes cover the ends of a cylindrical capsule [30]. These membranes are composed of the DE material between two compliant electrodes. The ball rolls freely in the capsule due to an initial external excitation, as shown in Fig. 1. The impact of the ball against one of the membranes causes its deformation, driving a capacitance change between the initial and deformed stated, leading to the energy harvesting. Thus, in the proposed concept the impacts become the primary energy harvesting mechanism by converting the kinetic energy to potential energy of the deformed membrane and then to the electrical energy. The two main advantages of the DE materials, used as the membranes, are their ability to stretch 300%–700% without tearing and their high dielectric permittivity relative to that of air. Both of these factors substantially increase the energy harvesting capacity of devices that utilize the DE material. While there remain issues related to compliant electrodes, which have to stretch as much as the DE membrane to keep the capacitor intact, this question lies outside of this paper's scope.

With this design, the VI-EH dynamics correspond to that of an impact pair; that is, a two degree of freedom system where the capsule is forced externally, and the motion of the ball inside the capsule follows from the impacts with the capsule ends and other inertial forces such as gravity. In general, the impact pair is distinct from other systems with two-sided constraints, and one of the main differences is that the dynamics of the impact pair can be described by a single equation of motion with respect to their relative displacement. In contrast, another ball and capsule system has been studied as a self-propulsion mechanism, when the inner mass was excited instead of the capsule [46]. A series of papers consider a different impact pair mechanisms for earthquake damage mitigation, by considering the damped motion of a mass moving between two deformable barriers, all subject to external harmonic forcing. Experimental and numerical results are compared in the context where additional forces on the mass appear due to damping and contact with the barriers. [47–54]).

The restitution coefficient plays an important role in VI systems, serving not only as the energy damping mechanism, but also as a parameter governing the stability and dynamic behavior of various periodic regimes. Generally, the restitution coefficient is a complex parameter, which typically depends on material characteristics, the shapes, the surfaces and the relative sizes of the colliding objects. The effects of some of these parameters on the value of the restitution coefficient as the function of collision velocity were reported in [55]. Although non-deterministic behavior of the restitution coefficient was observed and reported in a number of investigations, including but not limited to [55–57], the restitution coefficient in dynamic problems is commonly treated as a constant. Within this approach the dynamical model is used to establish the influence of the restitution coefficient on the system dynamics and related stability. Similarly, to the best of the authors' knowledge, the vast majority of published papers on two-sided VI oscillators have considered identical values of the restitution coefficient at opposite sides in their analytical and numerical studies.

While the common approach is to use constant restitution coefficients, there are sources of variation and asymmetry that may be included in the model. In some materials and models, the dependence of the restitution coefficient on relative impact velocity is more realistic [58–60]. Because of the fabrication process of the DE membranes in the VI-EH device, it is possible to pursue a design where the membranes have different mechanical properties. Moreover, the presence of compliant electrodes and the Maxwell stresses induced by the application of voltage can influence the membrane property [61], and its operating restitution coefficient value may be changed accordingly. All of these settings illustrate opportunities for introducing and controlling the restitution coefficient values of the membranes on the opposite sides of the capsule. The possibilities point to one of the main motivations of this study, namely, to explore how the asymmetric values of the restitution coefficient, employed within a single two-sided VI device, influence its dynamics and resulting energy output. Note that we do not consider a specific source of this asymmetry; rather, we pursue a general exploration of asymmetry in restitution coefficients to demonstrate its influence on the dynamics of the impact pair and the resulting energy output for the VI-EH device.

Previous analytical studies [62,63] have shown how asymmetries naturally appear in the regular periodic behaviors of the VI-EH device for given sets of parameters, as well as from other symmetry-breaking bifurcations. This raises the question of whether asymmetric restitution coefficients can be used to an advantage in these systems. Yet, it is not immediately obvious why or how asymmetric restitution coefficients may be beneficial, which we denote as r_T and r_B for impacts on the top and bottom membranes, respectively. The influence of the bifurcation structure on energy output in the VI-EH device, explored in [62,63], provides some direction for exploring advantageous asymmetries. As demonstrated in this previous work, both period doubling bifurcations and grazing play important roles in the proposed VI-EH pair leading to transitions between different stable periodic solutions. In some cases such a transition immediately reduces the energy harvesting performance of the device, which obviously is not beneficial. Grazing impacts in particular can deteriorate the system performance since grazing, by definition, implies a zero velocity impact, which produces no membrane deformation and consequently does not generate any power.

By understanding the nonlinear dependence of the system on r_T and r_B, we provide both quantitative and qualitative analyses of the influence of this asymmetry on the location of the bifurcations, thus indicating paths for improved performance of the energy harvesting device. For example, adjustable r_T and r_B can stimulate the system, via the nonlinear response, to remain in or transition to a favorable regime that generates more energy.

The value of the analysis follows from a number of non-intuitive results that influence energy output. First we find that while the smaller restitution coefficient leads to a reduced relative velocity immediately

following the impact, it also changes other important characteristics of the behavior, such as the phase differences between impacts and external forcing. Then it can result in a net gain of the impact velocities, and thus improve the energy output. Furthermore, we find that the asymmetry can extend the range of parameters where stable regular periodic behavior provides desirable energy output. With a larger stability range, the regular behavior is robust to perturbations or transitions to chaotic behavior, thus providing more reliable energy output. We explore new features that are related to asymmetry in r_T and r_B when combined with other parameters. For example, we identify several detrimental parameter combinations that contribute to low energy output, usually in terms of inclination angle. These observations also lead us to propose adjustments to the asymmetric restitution coefficients that may counteract the negative effects of inclination angle (or other parameters).

This paper has the following structure. In Section 2, we give the dimensional VI-EH model, and non-dimensionalize it to streamline the analysis. We also summarize the previous results for symmetric $r_T = r_B$, illustrating the influence of bifurcations on the energy output and motivating the study of asymmetry. In Section 3 we provide the analytical results for asymmetric restitution coefficients, deriving the analytical expressions for simple periodic 1:1 motion, and providing the stability analysis. Comparing the analytical results for the asymmetric case both with numerical results and with those from the symmetric case, we highlight potential advantages and complexities generated by the asymmetries. These comparisons motivate more in-depth comparisons in Section 4 that consider the effect of asymmetric $r_T \neq r_B$ on the average energy output voltage. They are developed while also varying other important design parameters such as device size and inclination angle, given the interplay between them. These results illustrate several ways the analysis can be used to improve system performance. Throughout we demonstrate how the analysis agrees with numerical simulations, provides results such as bi-stability that may be missed in the simulations, and guides potential design questions.

2. The model and previous results

2.1. The VI-EH model

The model of the VI-EH device is presented in Fig. 1, with a capsule of mass M and a ball of mass m that can move freely inside the capsule. Both ends of the capsule are covered by DE membranes with compliant electrodes [30]. The capsule is excited by an external harmonic force $\mathcal{F}(\omega\tau + \varphi)$ with a period of $2\pi/\omega$. We assume that any inertial forces are negligible compared to the applied harmonic force, and therefore do not influence the motion of the capsule. Then the motion of the cylinder satisfies the equation

$$\ddot{X}(\tau) = \frac{\mathcal{F}(\omega\tau + \varphi)}{M}\,. \tag{1}$$

The motion of the ball moving inside the capsule satisfies the equation

$$\ddot{x}(\tau) = -g\sin\beta\,, \tag{2}$$

valid between collisions of the ball with either of the membranes. Here $g = 9.8$ m/s^2 is the gravitational constant.

The notation x^- and X^- ($\dot{x}^-$ and $\dot{X}^-$) represents the positions (velocities) of the ball and capsule, respectively, before an impact, and x^+ and X^+ ($\dot{x}^+$ and $\dot{X}^+$) the positions (velocities) of the ball and capsule after the impact. We take r_B (r_T) as the coefficient of restitution for the bottom ∂B (top ∂T) of the capsule to allow for a design where the membranes have different properties. We assume that the impact of the ball does not affect the motion of the cylinder, $\dot{X}^- = \dot{X}^+$ and $X^- = X^+$, with m negligible compared to M. Then the impact condition yields the expression for the velocity of the ball after impact,

$$\dot{x}^+ = -r_B\dot{x}^- + (1 + r_B)\dot{X} \text{ for } x^+ = x^- = \partial B,$$

$$\dot{x}^+ = -r_T\dot{x}^- + (1 + r_T)\dot{X} \text{ for } x^+ = x^- = \partial T\,. \tag{3}$$

Here we take an instantaneous impact condition, where the duration of the impact is negligible, so that $x^+ = x^-$. For s the length of the capsule, $x = X - s/2$ ($x = X + s/2$) at the impact on ∂B (∂T).

Next, for efficient analysis of the influence of the parameters, it is useful to introduce the non-dimensionalized spatial and temporal variables,

$$X(\tau) = \frac{\|\mathcal{F}\|\pi^2}{M\omega^2}X^*(t)\,, \qquad x(\tau) = \frac{\|\mathcal{F}\|\pi^2}{M\omega^2}x^*(t)\,, \qquad \tau = \frac{\pi}{\omega}t\,. \tag{4}$$

As a result, a non-dimensionalized capsule length d depends on the dimensional length s, as well as on the forcing amplitude A and frequency ω,

$$d = \frac{M\omega^2}{A\pi^2}s, \quad \text{where} \quad A = \|\mathcal{F}\|. \tag{5}$$

Throughout this paper we fix the parameters $M = 124.5$ g as in [30] and $\omega = 5\pi$ Hz.

Since the proposed device as shown in Fig. 1 presents a vibro-impact pair, where both components can move relative to each other, it is reasonable to facilitate the dynamical analysis by introducing the relative position and velocity variables

$$Z = X^* - x^*, \qquad \dot{Z} = \dot{X}^* - \dot{x}^*\,. \tag{6}$$

Then the equations of motion in terms of the non-dimensionalized, relative variables are

$$\ddot{Z} = \ddot{X}^* - \ddot{x}^* = f(t) + \bar{g}, \quad \text{where} \tag{7}$$

$$f(t) = A^{-1}\mathcal{F}(\pi t + \varphi)\,, \qquad \|f\| = 1\,, \quad \text{and} \quad \bar{g} = \frac{Mg\sin\beta}{A}, \tag{8}$$

$$\dot{Z}_k^+ = -r_B\dot{Z}_k^- \text{ at } Z_k = \frac{d}{2} \quad (\text{impact at } \partial B) \tag{9}$$

$$\dot{Z}_k^+ = -r_T\dot{Z}_k^- \text{ at } Z_k = -\frac{d}{2} \quad (\text{impact at } \partial T)\,. \tag{10}$$

The notation $Z_k = X^*(t_k) - x^*(t_k)$ indicates the relative position at the kth impact taking place at $t = t_k$, and similarly for $\dot{Z}_k$. To obtain the equations of motion in between impacts we integrate (7) for $t \in (t_k, t_{k+1})$,

$$\dot{Z}(t) = -r\dot{Z}^-(t_k) + \bar{g}(t - t_k) + F_1(t) - F_1(t_k) \tag{11}$$

$$Z(t) = Z_k^- - r\dot{Z}_k^-(t - t_k) + \frac{\bar{g}}{2}(t - t_k)^2 + F_2(t) - F_2(t_k) - F_1(t_k)(t - t_k)\,, \tag{12}$$

where $F_1(t) = \int f(t)\,dt$ and $F_2(t) = \int F_1(t)\,dt$.

Once the impact velocity is found, the output voltage of the VI-EH device can be directly determined from the deformation of the membrane. In order to focus this paper on the mechanical dynamics, we use a separate model for calculating the electrical output. Using a simple geometry, this model accounts for the membrane deformation over time, and provides expressions for the changes in the membrane capacitance. We then determine the output at the impact instance. Of course, in the full system the voltage will be collected over a short but finite time interval, but this instantaneous approximation is sufficient for providing a picture of how the dynamics influences the output voltage.

For a constant input voltage U_{in} applied to the membranes, U_k^{imp}, the voltage generated by the membrane deformation at the kth impact, is determined as

$$U_k^{\text{imp}} = \left[\frac{A_k}{\pi R_c^2}\right]^2 U_{\text{in}}\,, \tag{13}$$

where R_c is the radius of the undeformed membrane and A_k is the area of the membrane at the deformed state [30] given by

$$A_k = 2\pi R_b^2(1 - \cos\alpha_k) + \frac{\pi R_c^2 - \pi(R_b\sin\alpha_k)^2}{\cos\alpha_k}\,, \tag{14}$$

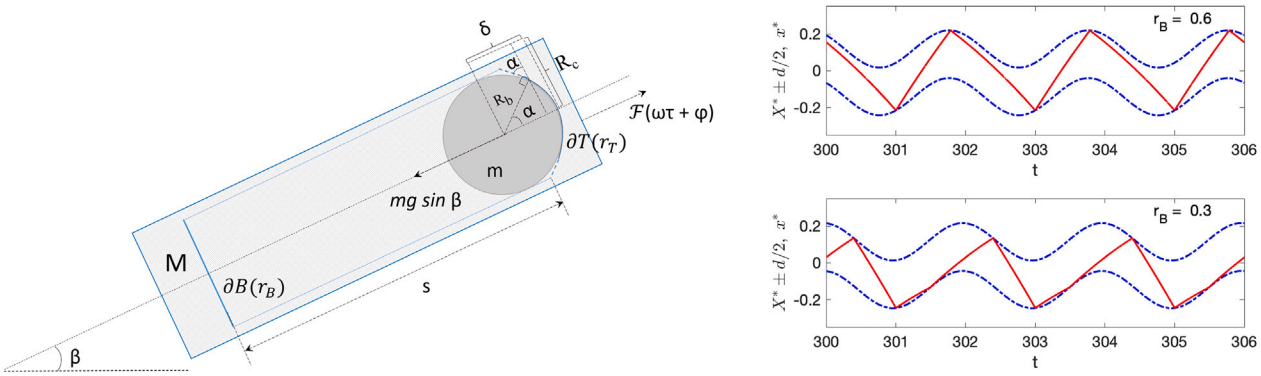

Fig. 1. Left: Schematic for the vibro-impact energy harvester. Parameters shown are: $M(m)$, the mass of the cylinder (ball); β, the angle of incline; s the length of cylinder; $\partial B(\partial T)$, the bottom (top) membrane; $\mathcal{F}(\omega\tau+\varphi)$ a harmonic excitation, $mg\sin\beta$ the force due to gravity; R_b, the radius of the ball, R_c, the active radius of the membrane, δ, the largest deflection of the membrane at impact, α, the angle of deflection. Right: Illustration of typical motions of the ball (red solid line) within the capsule (blue dashed lines) in terms of the non-dimensional variables, with one (two) impact(s) on ∂B and one on ∂T per period of the forcing, for larger (smaller) r_B. Other parameters are strength of forcing $A = \|\mathcal{F}\| = 5$ N, $\beta = \pi/6$, $r_T = 0.5$.

for R_b the radius of the ball. The angle α_k at the kth impact depends upon the value of the largest deformation of the membrane center δ_k, as follows:

$$\cos\alpha_k = \frac{-2R_b(\delta_k - R_b) + 2R_c\sqrt{R_c^2 + \delta_k^2 - 2\delta_k R_b}}{2[R_c^2 + (\delta_k - R_b)^2]}$$

$$\delta_k = \left[\frac{\nu+1}{2K} m V_k^2\right]^{\frac{1}{\nu+1}}. \tag{15}$$

Note that δ_k depends on the parameters of the elastic force of the membrane K, ν and the relative dimensional velocity at the kth impact, V_k, proportional to $\dot{Z}_k$. The thickness of the membrane in the deformed state is recalculated based on the conservation of mass, thereby it allows calculating the change in the capacitance between the initial and deformed states. In the remainder of this paper we fix the values of the following parameters: $K = 4.0847 \cdot 10^5$ and $\nu = 2.6$, $R_b = 5$ mm, $R_c = 6.3$ mm. Note that in applications the range of voltages used in actuators and energy harvesting is 1000–8000 V [64], and in this paper we use $U_{\text{in}} = 2000$V.

We investigate and compare the behavior of the absolute output voltage at the kth impact, U_k, as well as two different averages of the output voltage, average per impact $\overline{U}_I$ and average over time $\overline{U}_T$, defined as

$$U_k = U_k^{\text{imp}} - U_{\text{in}}, \qquad \overline{U}_I = \frac{\sum_{k=1}^N U_k}{N}, \qquad \overline{U}_T = \frac{\sum_{k=1}^N U_k}{t_f - t_0}. \tag{16}$$

Here N is the number of impacts within a time interval $[t_0, t_f]$ and $t_f - t_0 = \frac{\omega}{\pi}(\tau_f - \tau_0)$ is the corresponding non-dimensionalized time interval. We average over this non-dimensionalized time interval for ease in comparing $\overline{U}_I$ and $\overline{U}_T$ on the same plot.

2.2. Framework and notation

Following the notation introduced in [63] for a T-periodic external excitation, we categorize different periodic motions in the VI-EH system by the notation n:m/pT, with n(m) being the number of impacts against the bottom (top) of the capsule per period pT, simplifying to just n:m in the cases when $p = 1$. The linear stability analysis and conditions for transition from 1:1 to 2:1 and from 2:1 to 3:1 motion has been established in [62,63] for $r_T = r_B$. Moreover, for this symmetric case it has been shown that the averaged output energy per impact is higher in 1:1 than in 2:1 and 3:1 regimes. The results are in terms of the key parameters summarized in Table 1.

In particular we focus on semi-analytical representations of 1:1 periodic motions in the case of asymmetric restitution coefficients, from which we obtain their bifurcation structure and stability. These results indicate several directions for design advantages, since the analysis demonstrates both benefits and limitations of the asymmetry. This leads to studying bifurcations of new 1:2 asymmetric solutions that have not been observed in previous studies with symmetric $r_T = r_B$. We see that the results for energy output are dependent on the restitution ratio r_B/r_T, as well as the magnitudes of r_T, r_B combined with the inclination angle β, through which the asymmetric effect of gravity plays a role.

Furthermore, we find that there are two types of regular 1:1 periodic motion in the asymmetric case. Again, the identification and analysis of these different periodic motions leads to an exploration of energy output varying non-monotonically with the ratio r_B/r_T specifically near the transition between different 1:1 solutions. The analysis also points to the bi-stability of these two types of 1:1 solutions which can lead to more complex behavior overall. Thus we indicate the potential benefits system energy output, obtained through the influence of asymmetric r_T and r_B on the period doubling and grazing bifurcations, as well as on the (bi)-stability of periodic motions in general.

2.3. Symmetric restitution coefficients $r_B = r_T$

We illustrate the type of bifurcations that occur in the solutions to (7)–(10), treating d as the bifurcation parameter. Results are shown for both impact velocity and average output energy per impact, comparing numerical results with analytical results as in [62,63]. Comparisons within the symmetric case of $r_B = r_T = r$ motivates the investigation of the asymmetric case $r_B \neq r_T$.

The top row of Fig. 2 shows the bifurcation diagrams for different attracting solutions represented by the impact velocity $\dot{Z}_k$ vs. the non-dimensional length d, (5). The bottom row shows the output voltage at impact U_k (16) and the average output voltage per impact $\overline{U}_I$ (16) corresponding to the branches of $\dot{Z}_k$ shown in the top row. Here the numerical results are obtained by a continuation-type method, choosing a value of d, computing over a sufficiently long time to reach the attracting behavior, from which we obtain the sequence of values of $\dot{Z}_k$ at that value of d. This attracting behavior provides the initial condition in the computation for the next value of d, typically close to the previous one. Recalling from (5) that d varies linearly with s, and is inversely proportional to A, Fig. 2 shows results for d decreasing, with either decreasing dimensional capsule length s or increasing forcing amplitude A. As the impact velocity increases with A, we observe the nonlinear increase with decreasing d in panels (f) and (h) due to the nonlinear relationship between d and A. Note here that with the increased A, the influence of the gravity force is effectively reduced, as follows from the non-dimensional analysis (8), so that the grazing bifurcation G is reached in (d), (h) without period doubling.

These graphs illustrate a number of possible transitions for the 1:1 solutions; A_1 indicates a change in local behavior, where the 1:1

Table 1
Parameters and variables of the VI-EH system.

Parameters/Variables	Description
$M = 124.5$ g ($m = 3.5$ g)	Mass of the capsule (ball)
β	Angle of capsule incline
s (d)	Dimensional (non-dimensionalized) capsule length
$\mathcal{F}(\omega\tau + \varphi)$	External harmonic force with a period of $2\pi/\omega$, frequency $\omega = 5\pi$ Hz and the phase shift φ in (1)
$A = \|\|\mathcal{F}\|\|$	Excitation amplitude $\mathcal{F}$ in (4), (5).
r_B (r_T)	Coefficient of restitution for the bottom ∂B (top ∂T) membrane of the capsule
$g = 9.8$ m/s^2	Gravitational constant
$\ddot{X}(\tau)$, $\dot{X}(\tau)$, $X(\tau)$ ($\ddot{x}(\tau)$, $\dot{x}(\tau)$, $x(\tau)$)	Acceleration, velocity, position of the capsule (ball)
V_k	Relative dimensional velocity at the kth impact in (15)
$\ddot{Z}(t)$, $\dot{Z}(t)$, $Z(t)$	Non-dimensionalized, relative acceleration, velocity, position of the ball
U_k^{imp} (U_k)	Voltage generated by the membrane deformation (absolute output voltage) at the kth impact in (13), (16)
$\overline{U}_I$ ($\overline{U}_T$)	Averaged output voltage per impact (over time) in (16)
$U_{\text{in}} = 2000$ V	Constant input voltage applied to the membranes
$R_c = 6.3$ mm	Radius of the undeformed membrane
A_k	Area of the membrane at the deformed state in (14)
$R_b = 5$ mm	Radius of the ball
α_k	Angle at the kth impact in (15)
δ_k	Largest displacement of the membrane center at the kth impact in (15)
$K = 4.0847 \cdot 10^5$, $\nu = 2.6$	Parameters of the elastic force of the membrane

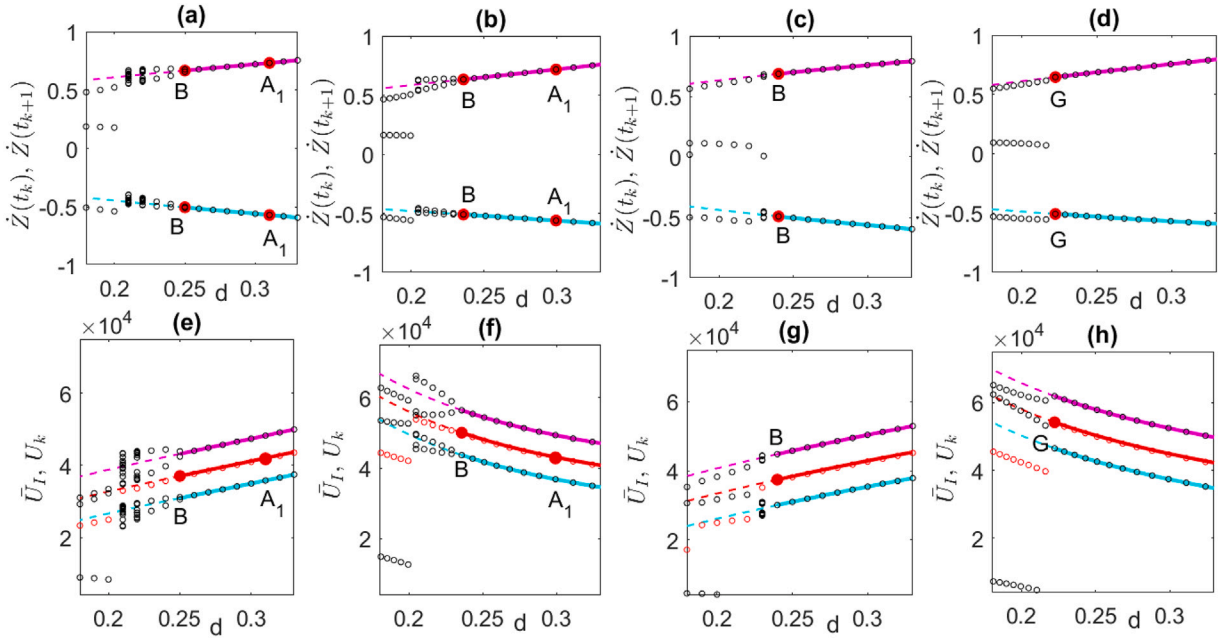

Fig. 2. Bifurcation diagrams for $\beta = \pi/6$. In (a) and (c) for $r = 0.5$ and $r = 0.25$, respectively, we show the impact velocities for $0.29 < s < 0.53$ m and $A = 5$ N, while in (b) and (d) for $r = 0.5$ and $r = 0.25$ we show the impact velocities for $4.72 < A < 8.64$ N and $s = 0.5$ m. The output voltages for (a)–(d) are below them in (e)–(h). Numerical results are shown by open black circles for $\dot{Z}_k$ in the top row, and in the bottom row by black (red) circles for U_k ($\overline{U}_I$). Analytical results for $\dot{Z}_k$, U_k, and $\overline{U}_I$ based on results of [62] for 1:1 periodic solutions are shown by magenta (impact on ∂B) and cyan (impact on ∂T) lines, with solid (dashed) lines corresponding to stable (unstable) solutions. Points A_1 indicate transitions from stable focus to stable node of the 1:1 solution. B indicates period doubling bifurcation to $1{:}1/2T$. Points marked with G correspond to grazing transition from 1:1 to 2:1 periodic behavior (two impacts with $\dot{Z}_k > 0$ on ∂B, one impact with $\dot{Z}_k < 0$ on ∂T.). (For interpretation of the references to color in this figure legend, the reader is referred to the web version of this article.)

solution changes from a stable focus to a stable node, B indicates a period doubling bifurcation to $1{:}1/2T$, while G indicates the grazing transition from 1:1 to 2:1 behavior, with two impacts on ∂B with $\dot{Z} > 0$, followed by an impact on ∂T with $\dot{Z}_k < 0$. This grazing transition is described further below. These cases and other transitions to 2:1 periodic motion have been studied both analytically and numerically in [62,63], using a linear stability analysis similar to that shown in Section 3.3.

We highlight a few observations that motivate the analysis of the next sections. At the period doubling of 1:1 solutions we do not see a dramatic drop in $\overline{U}_I$, since the impact velocities do not change dramatically at the transition to $1{:}1/2T$ behavior. However, when solutions transition from $1{:}1/pT$ solutions to 2:1 solutions, there is a noticeable drop in $\overline{U}_I$ due to the second low velocity impact on ∂B in the 2:1 behavior. For smaller values of r, we note that the transitions from $1{:}1/pT$ to 2:1 are shifted to larger values of d (compare e.g. panels (a) and (c)). Panel (d) illustrates a direct transition from 1:1 to 2:1 behavior via a grazing bifurcation marked G, without period doubling of the 1:1 solution. While it may seem counter-intuitive that $\overline{U}_I$ is comparable for the two different values of r shown, this follows from the phase shift of the impacts relative to the oscillatory forcing, which directly influences $\dot{Z}_k$ and U_k.

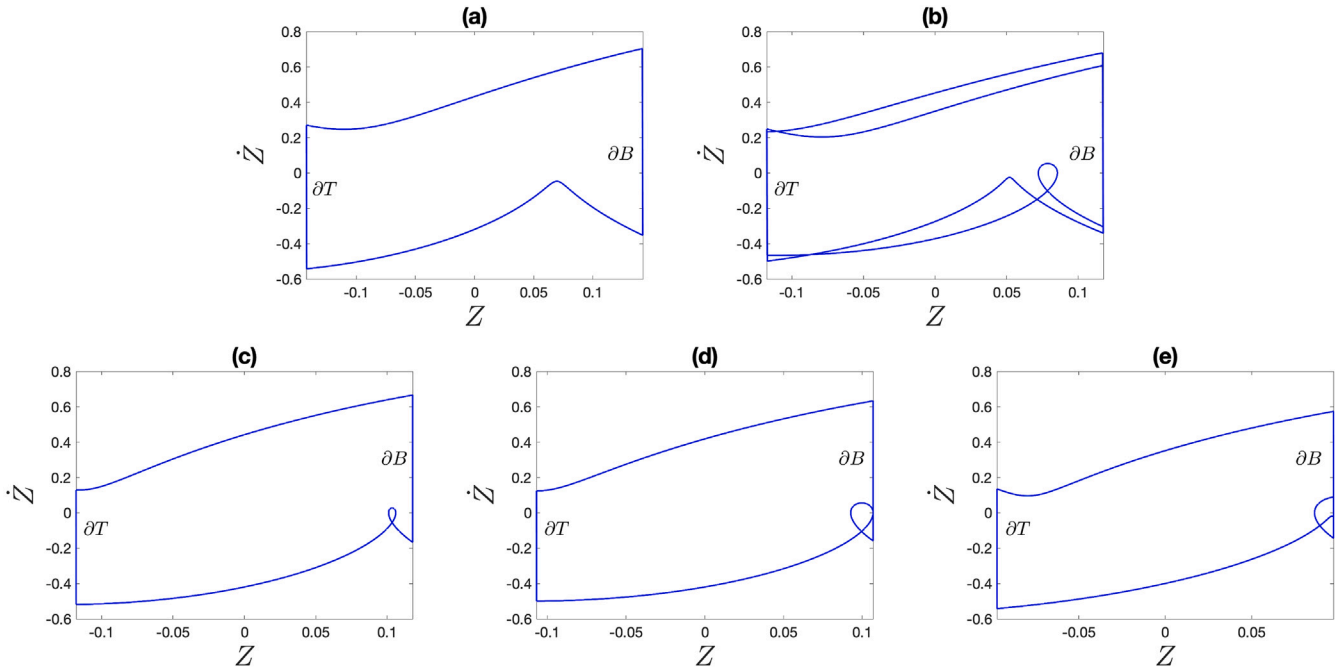

Fig. 3. Periodic solutions shown in the phase plane, with $Z = d/2$ ($Z = -d/2$) corresponding to impacts on ∂B (∂T). Upper: Periodic solutions for $r = 0.5$, corresponding to the branches shown in Fig. 2(a) with $A = 5$ N, for (a) $d = .28$ with stable 1:1 periodic motion, and (b) $d = .23$ with stable 1:1/2T motion. Lower: Phase planes for $r = 0.25$, corresponding to branches shown in Fig. 2(d); (c) $A = 6.6$ N, $d \approx .2358$ with stable 1:1 motion; (d) $A = 7.28$ N, $d \approx .2138$, corresponding to grazing at G; (e) $A = 8$ N, $d \approx .1945$, with stable 2:1 motion.

Fig. 3 provides phase plane plots that illustrate the period doubling behavior transition from 1:1 to 1:1/2T solutions and the route to 2:1 behavior via grazing. A linear stability analysis of 1:1 solutions [62] identifies period doubling bifurcations marked with B in Fig. 2, with Fig. 3(a),(b) showing phase plane trajectories for values of d on either side of this bifurcation. We note that even though the values of $\dot{Z}_k$ are relatively close for both the 1:1 (a) and 1:1/2T (b) behaviors, there is a difference in the phase shift of the impacts for the two different periodic solutions, which can also influence energy output. The dynamical route to 2:1 behavior is illustrated in Fig. 3(c)–(e), where the phase plane behavior for specific values of d taken from Fig. 2(d). As we can see from these figures, in the dynamical path from ∂B to ∂T, given by (11)–(12), $\dot{Z} > 0$ for a short interval. Then we observe that, following an impact at ∂B, the bottom of the capsule approaches the ball for these values where $\dot{Z} > 0$. Under certain conditions, this approach leads to a second impact at ∂B, with low relative $\dot{Z}_k$, as shown in Fig. 3(e). Grazing occurs at the time t_G where $\dot{Z}(t_G) = 0$ at this second impact, as shown in Fig. 3(d).

The phase plane plots in Fig. 3 indicate the importance of asymmetries in the 1:1 behavior; that is, asymmetries in the $\partial T \to \partial B$ and $\partial B \to \partial T$ motions can lead to transitions from 1:1 behavior to other behaviors. Furthermore, the drop in $\overline{U}_I$ at the transition to 2:1 behavior motivates seeking ways to limit or postpone such transitions. As one would expect intuitively, the asymmetry is more prevalent with larger inclination angle $\beta > 0$ given its influence on Z and $\dot{Z}$, as explored for $r_T = r_B$ in [63] and in on-going work [63]. In addition, contrasting Figs. 2 (c) and (d), one can see that the changes in s and A have different influences on the response. Besides the obvious effect that increasing A leads to high energy input into the system, it also can advance the grazing bifurcation labeled G, preempting period doubling as in Fig. 2(d). In contrast, decreasing s typically results in the period doubling before transitions to 2:1 behavior, except for very small r [65]. Given the complex combined influence of β, A, s, and r on the asymmetric motion, the associated bifurcations, and the resulting energy output U_k we seek a valuable analytical description of these behaviors and transitions. The asymmetries motivate new analyses for asymmetric values of $r_T \neq r_B$ for the opposing membranes, which points to design features that influence these transitions.

3. Analytical results for asymmetric $r_T \neq r_B$

3.1. Derivation of the analytical results

To identify the influence of asymmetric restitution coefficients r_T and r_B and $\dot{Z}$ and U_k, we derive analytical results for 1:1 periodic solutions. As shown in Fig. 2 for $r_T = r_B$, the results provide the bifurcation structure of $\dot{Z}$, the parameter ranges for 1:1 solutions, and the changes in U_k, $\overline{U}_I$, $\overline{U}_T$ related to different types of solutions. To obtain the analytical results for 1:1 behavior, we follow the approach used in [62]. By evaluating the Eqs. (11)–(12) at successive impact times t_k, we obtain two maps, P_1 corresponding to the transition from ∂B to ∂T, and P_2 for the transition from ∂T to ∂B. We focus here on 1:1/pT behavior, composed of alternating transitions described by P_1 and P_2. Then the time between the impacts for $P_1(P_2)$ is $T_1(T_2)$, where

$$T_1 = \Delta t_k = t_{k+1} - t_k,\ T_2 = \Delta t_{k+1} = t_{k+2} - t_{k+1}\,. \tag{17}$$

These maps, based on the time evolution given by (11)–(12), give expressions for the relative impact velocity $\dot{Z}_j$ and the position at impact $Z_j = \pm d$ in terms of the previous $\dot{Z}_{j-1}$,

$$P_1 : (Z_k \in \partial B, \dot{Z}_k, t_k) \to (Z_{k+1} \in \partial T, \dot{Z}_{k+1}, t_{k+1}),$$

$$\dot{Z}_{k+1} = -r_B \dot{Z}_k + \bar{g} T_1 + F_1(t_{k+1}) - F_1(t_k), \tag{18}$$

$$-d = -r_B \dot{Z}_k T_1 + \frac{\bar{g}}{2} T_1^2 + F_2(t_{k+1}) - F_2(t_k) - F_1(t_k) T_1. \tag{19}$$

$$P_2 : (Z_{k+1} \in \partial T, \dot{Z}_{k+1}, t_{k+1}) \to (Z_{k+2} \in \partial B, \dot{Z}_{k+2}, t_{k+2}),$$

$$\dot{Z}_{k+2} = -r_T \dot{Z}_{k+1} + \bar{g} T_2 + F_1(t_{k+2}) - F_1(t_{k+1}), \tag{20}$$

$$d = -r_T \dot{Z}_{k+1} T_2 + \frac{\bar{g}}{2} T_2^2 + F_2(t_{k+2}) - F_2(t_{k+1}) - F_1(t_{k+1}) T_2\,. \tag{21}$$

We seek analytical descriptions for 1:1 T-periodic behavior, where the forcing $f(t)$ is T-periodic. We combine the definitions of P_1 and P_2 together with the periodicity conditions

$$Z_{k+2} = Z_k, \qquad \dot{Z}_{k+2} = \dot{Z}_k, \qquad T = T_1 + T_2\,, \tag{22}$$

$$f(t) = f(t+T), \qquad F_1(t) = F_1(t+T), \qquad F_2(t) = F_2(t+T),$$

to get three different expressions for $\dot{Z}_k$. From these we can obtain the triple $(\dot{Z}_k, \varphi_k, \Delta t_k)$ that characterizes the 1:1 behavior. Specifically, without loss of generality we take the kth impact at ∂B as the initial impact of the 1:1 periodic solution. Then $\dot{Z}_k$ is its impact velocity, Δt_k is the time until the next impact (17), and φ_k =mod$(\pi t_k + \varphi, 2\pi)$ is the phase shift of the kth impact relative to the forcing $f(t)$. We add (18) and (20) and use (18) and (22) to get the first equation for $\dot{Z}_k$,

$$\dot{Z}_k = \frac{1}{1 - r_B r_T}\left[\bar{g}T - (1 + r_T)(\bar{g}T_1 + F_1(t_{k+1}) - F_1(t_k))\right]. \tag{23}$$

Similarly, we get the second equation for $\dot{Z}_k$ by adding (19) and (21) and using (18) and (22),

$$\dot{Z}_k = \frac{1}{r_B T_1 - r_B r_T T_2}\left[\frac{\bar{g}}{2}(T_1^2 + T_2^2) - r_T T_2(\bar{g}T_1 + F_1(t_{k+1}) - F_1(t_k)) - F_1(t_k)T_1 - F_1(t_{k+1})T_2\right]. \tag{24}$$

The third equation is obtained by rewriting (19)

$$\dot{Z}_k = \frac{1}{r_B T_1}\left[d + \frac{\bar{g}}{2}T_1^2 + F_2(t_{k+1}) - F_2(t_k) - F_1(t_k)T_1\right]. \tag{25}$$

From the system (23)–(25) we solve for the triple $(\dot{Z}_k, \varphi_k, \Delta t_k)$ in Matlab with the *vpasolve* function.

Alternately one can reduce the equations further for a specific choice of $f(t) = \cos(\pi t + \varphi)$ with period $T = 2$. Then it is possible to get explicit expressions for $\dot{Z}$ and φ_k in terms of Δt_k. In seeking $1{:}1/pT$ periodic solutions, it is convenient to introduce the parameter $0 \le q \le 1$ as follows

$$T_1 = 2pq \text{ and } T_2 = 2p(1-q), \tag{26}$$

for $q = \Delta t_k/2$, and $p = 1$ for 1:1 periodic solutions. Additionally we take, without loss of generality, $t_k = 0$ and $\varphi_k = \text{mod}(\varphi, 2\pi)$. Details are provided in Appendix A.1, which we summarize here.

Combining (18)–(20) and using the periodic conditions (22), leads to (34), which, for this specific forcing, simplifies to

$$\dot{Z}_k = \frac{2\bar{g}}{r_B + \zeta}\left(q - \frac{1}{r_T + 1}\right) + \frac{\sin(2\pi q + \varphi) - \sin(\varphi)}{\pi(r_B + \zeta)}, \tag{27}$$

where $\zeta = -\frac{1+r_B}{1+r_T}$. Similarly, (35) reduces to the equation for φ,

$$\varphi = \arcsin\left[\frac{\pi}{2}\dot{Z}_k\lambda - \pi\bar{g} + 2\pi q\bar{g}\right], \tag{28}$$

where $\lambda = 2(q-1)(r_T\zeta + r_B + \zeta) - 2qr_B$. Finally, we add Eqs. (19) and (21), using periodic conditions, and substitute in the previous equations. The result is combined with (19), then squared, and added to the square of (27) to obtain a quadratic equation for $\dot{Z}_k$:

$$\left[2\bar{g}q^2 - 2\bar{g}q - d + 2qr_B\dot{Z}_k + q\lambda\dot{Z}_k\right]^2 \cdot \pi^4 + \left[\dot{Z}_k(r_B + \zeta) - 2\bar{g}\left(q - \frac{1}{r_T + 1}\right)\right]^2 \cdot \pi^2 = 2 - 2\cos(2\pi q). \tag{29}$$

From this result we have an explicit expression for $\dot{Z}_k = \frac{-b \pm \sqrt{b^2 - 4ac}}{2a}$, where a, b, and c are given in (39)–(41). From (27)–(29) we then have equations for Z_k and φ_k in terms of q, from which we can identify the triple $(Z_k, \varphi_k, \Delta t_k)$. Note that for $r_T = r_B$, the system (27)–(29) reduces to the system in [62], used to obtain analytical results for 1:1 periodic solutions with symmetric restitution coefficients. Then, from either (23)–(25) or (27)–(29) we can solve for the triple $(\dot{Z}_k, \varphi_k, \Delta t_k)$ for varying values of d. Results are shown in Fig. 4, as well as for the corresponding output voltages at impact U_k and averaged over impacts $\bar{U}_I$ (16).

3.2. Comparisons of the analytical results

We compare the analytical results derived above for $r_T \neq r_B$ to simulations of the full model (1)–(3) and to the symmetric results for $r_B = r_T$ shown in Section 2.3. In this section we treat d as the bifurcation parameter, as in Fig. 2. These initial results show novel behaviors for the asymmetric case, potentially valuable for the energy output. These results then motivate the more comprehensive exploration of Section 4.

In Fig. 4 we compare the analytical results for the 1:1 periodic solution based on (23)–(25) with numerical results from (1)–(3). We show the case of $r_T = .5$ and two different values of $r_B \neq r_T$. Here the numerical results are obtained again by a continuation-type method for decreasing d, as described in Section 2.3. Comparing with $r_T = r_B$ shown in Fig. 2(a)–(b), for smaller $r_B < r_T$ we see that the period doubling and transitions to 2:1 behavior occur for larger d, as shown in Fig. 4(a)–(b). For $r_B > r_T$, the transition to $1{:}1/pT$ occurs for smaller d than for the case with $r_B = r_T$ (e.g. compare Fig. 2(c) and Fig. 4(c)). Furthermore, for d decreasing with increasing A, the shift in the period doubling to $1{:}1/2T$ can be large enough so that it is preempted by the 1:2 transition (see G in Fig. 4(d)). Below we explore ranges of r_B over which similar results hold.

The time series in Fig. 5(a)–(c) with fixed $r_T = .5$ further illustrate that different r_B values can shift the bifurcations and thus change U_k. These figures show the non-dimensionalized absolute positions of the cylinder X^* and the ball x^*. Panel (a) shows that for $r_B < r_T$ ($r_B = .45$), the impact on ∂B occurs near the minimum of X^*, corresponding to a small phase shift φ. Following the impact, the velocity of the ball $\dot{x}^*$ is near that of the capsule $\dot{X}^*$, allowing a second impact on ∂B to occur shortly after the first, corresponding to 2:1 behavior. For larger r_B, there is a larger velocity $\dot{x}^*$ following the impact with ∂B, resulting from the larger value of impact velocity $\dot{Z}_k$ and, in some scenarios, a larger phase shift φ_k, yielding either $1{:}1/2T$ motion as shown in Fig. 5(b), or 1:1 periodic motion as shown in Fig. 5(c). The transition to 2:1 (1:2) periodic solutions for $r_B < r_T$ ($r_B > r_T$) yields an additional small positive (negative) impact velocity on ∂B (∂T) per period, as in Fig. 5(a) for 2:1 solutions. The transition for $r_B > r_T$ to 1:2 periodic behavior is not shown, but from Fig. 5(c) we can observe that this second impact is possible with larger r_B. The bifurcation diagrams in Fig. 4(d),(h) show the $\dot{Z}_k$ and U_k for 1:2 periodic solutions, obtained numerically for values of d below the point G.

The bottom row of Fig. 4 provides U_k and $\overline{U}_I$ corresponding to the $\dot{Z}_k$ shown in the top row. As in Fig. 2 for the symmetric case, $\overline{U}_I$ has a notable drop following transitions to 2:1 periodic solutions, and similarly for transitions to 1:2 periodic solutions as in Fig. 4(h). In both cases these transitions yield an additional impact, with small $|\dot{Z}_k|$. Comparing panels (a) and (c) in Fig. 4, we observe that the 2:1 transition is shifted to smaller d for larger r_B. Similarly for the setting where d decreases with A as in (b) and (d), yielding a larger range of d with 1:1 solutions for larger r_B, and thus a larger increase in $\overline{U}_I$ with A. Fig. 5(d) compares the decrease (increase) of $\overline{U}_I$ ($\overline{U}_T$) for the different values of r_B shown in Fig. 5(a)–(c). Again we see that for larger r_B, the transition to 2:1 or 1:2 behavior from 1:1 or $1{:}1/pT$ occurs for smaller values of d. As defined in (16), $\overline{U}_I = \overline{U}_T$ for the 1:1 solution, which is observed over a larger range of d for $r_B = .6$. Note that the transition to 1:2 behavior for $r_B = .6$ results in lower energy output for both $\overline{U}_I$ and $\overline{U}_T$, as compared with the respective average output values for the 2:1 behavior obtained for smaller r_B. This difference between 1:2 and 2:1 solutions follows from the fact that 1:2 solutions have an additional impact on ∂T with lower $|\dot{Z}_k|$ as compared with the additional impact at ∂B for 2:1 solutions.

3.3. Linear stability analysis for asymmetric $r_T \neq r_B$

Certain critical points for the 1:1 solutions in the bifurcation diagrams are obtained by a linear stability analysis around the triples $(\dot{Z}_k, \varphi_k, \Delta t_k)$. At these points we observe different types of linear stability for these solutions.

We take $\delta\mathbf{H}_k$ to be a small perturbation to the fixed point $\mathbf{H}_k^* = (t_k, Z_k)$ of the map $P = P_1 P_2$, corresponding to 1:1 solutions with period

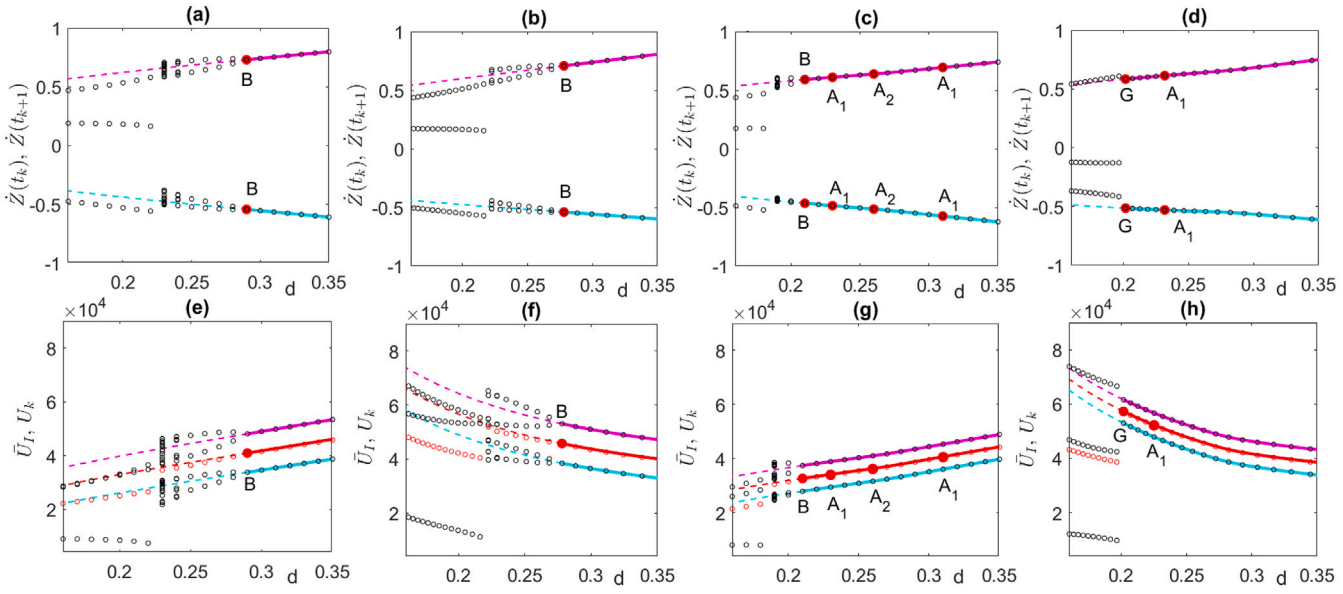

Fig. 4. Bifurcation diagram for the impact velocity $\dot{Z}_k$ (a)–(d) and output voltages $\bar{U}_I, U_k$ (16)(e)–(h) for $\beta = \pi/6$, $r_T = 0.5$, and (a), (e) $r_B = 0.45$, $A = 5$ N, $0.257 < s < 0.643$ m; (b), (f) $r_B = 0.45$, $3.89 < A < 9.73$ N, $s = 0.5$ m; (c), (g) $r_B = 0.59$, $A = 5$ N, $0.257 < s < 0.643$ m, (d), (h) $r_B = 0.59$, $3.89 < A < 9.73$ N, $s = 0.5$ m. Numerical results are shown by open black circles for $\dot{Z}_k$ in the top row, and in the bottom row by open black (red) circles for U_k ($\overline{U}_I$). Analytical results for $\dot{Z}_k$, U_k, and $\overline{U}_I$, based on results for 1:1 periodic solutions from (23)–(25), are shown by magenta (impact on ∂B) and cyan(impact on ∂T) lines, with solid (dashed) lines corresponding to stable (unstable) solutions. Points A_1, A_2, B are obtained from the linear stability analysis in Section 3.3. Point G corresponds to the transition from 1:1 to 1:2 behavior via grazing. Note 1:2 periodic solutions are characterized by two impacts with $\dot{Z}_k < 0$ on ∂T, and one impact with $\dot{Z}_k > 0$ on ∂B. (For interpretation of the references to color in this figure legend, the reader is referred to the web version of this article.)

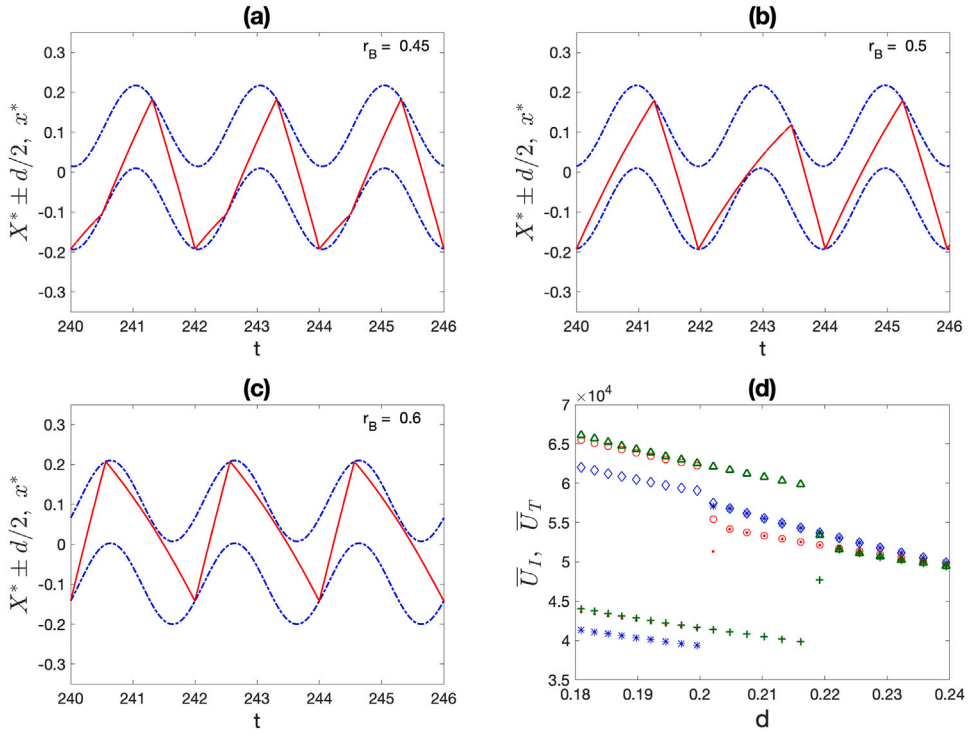

Fig. 5. Time series (a)–(c) illustrating the effect of different r_B, with $A = 7.5$N, ($d = .2075$), on the motion of the ball (red solid line) within the capsule (blue dashed lines). (a) $r_B = 0.45$, yields stable 2:1 behavior; (b) $r_B = 0.5$ yields stable $1{:}1/2T$ behavior; (c) $r_B = 0.6$ yields stable 1:1 behavior. In (d) we compare the average energy outputs $\overline{U}_I$ and $\overline{U}_T$ for $r_B = 0.6$, (blue $*$ and diamonds), for $r_B = 0.5$, (red . and o), and for $r_B = 0.45$, (green + and triangles), with A varying, $s = 0.5$m. The abrupt decrease (increase) in $\overline{U}_I$ ($\overline{U}_T$) corresponds to the transition to 2:1 behavior for $r_B = 0.45$ and $r_B = 0.5$ and to 1:2 behavior for $r_B = 0.6$. $r_T = 0.5$, $\beta = \pi/6$, $s = 0.5$ m for (a)–(d). (For interpretation of the references to color in this figure legend, the reader is referred to the web version of this article.)

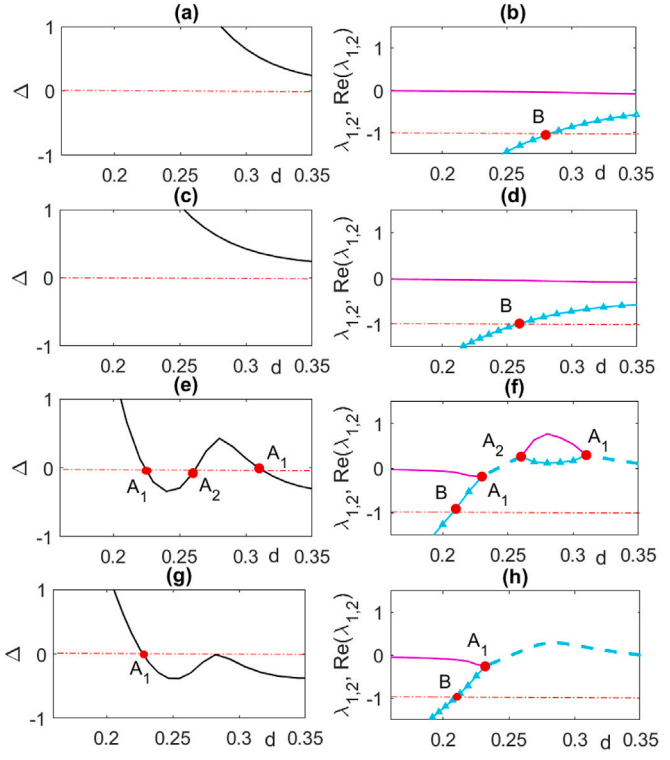

Fig. 6. Linear stability analysis based on Δ and the eigenvalues $\lambda_{1,2}$ of the matrix DP for the examples shown in Fig. 4, with $\beta = \pi/6$ and $r_T = 0.5$(a)–(b) $r_B = 0.45$, $A = 5$ N, $0.257 < s < 0.643$ m; (c)–(d) $r_B = 0.45$, $r_T = 0.5$, $3.89 < A < 9.73$ N, $s = 0.5$ m; (e)–(f) $r_B = 0.59$, $A = 5$ N, $0.257 < s < 0.643$ m; (g)–(h) $r_B = 0.59$, $3.89 < A < 9.73$ N, $s = 0.5$ m. Real eigenvalues $\lambda_{1,2}$ are shown with magenta lines and cyan lines with triangles. For complex eigenvalues, the real part $\mathrm{Re}(\lambda_{1,2})$ is shown with cyan dashed lines. Red dash-dotted lines indicate $\Delta = 0$ and $\lambda_j = -1$ for reference. Points marked A_1, (A_2) indicate transitions of the fixed point from (to) stable focus to (from) stable node for decreasing d, and B indicates a period doubling instability. (For interpretation of the references to color in this figure legend, the reader is referred to the web version of this article.)

T. Linearizing about $\delta\mathbf{H}_k = 0$, we obtain the following equation for $\delta\mathbf{H}_{k+2}$:

$$\delta\mathbf{H}_{k+2} = DP(\mathbf{H}_k^*)\delta\mathbf{H}_k = DP_2(\mathbf{H}_{k+1}^*)\cdot DP_1(\mathbf{H}_k^*)\,\delta\mathbf{H}_k\,, \tag{30}$$

with

$$DP(\mathbf{H}_k^*) = DP_2(\mathbf{H}_{k+1}^*)\cdot DP_1(\mathbf{H}_k^*) = \begin{bmatrix} \frac{\partial t_{k+2}}{\partial t_{k+1}} & \frac{\partial t_{k+2}}{\partial \dot{Z}_{k+1}} \\ \frac{\partial \dot{Z}_{k+2}}{\partial t_{k+1}} & \frac{\partial \dot{Z}_{k+2}}{\partial \dot{Z}_{k+1}} \end{bmatrix}_{\mathbf{H}_{k+1}=\mathbf{H}_{k+1}^*} \cdot \begin{bmatrix} \frac{\partial t_{k+1}}{\partial t_k} & \frac{\partial t_{k+1}}{\partial \dot{Z}_k} \\ \frac{\partial \dot{Z}_{k+1}}{\partial t_k} & \frac{\partial \dot{Z}_{k+1}}{\partial \dot{Z}_k} \end{bmatrix}_{\mathbf{H}_k=\mathbf{H}_k^*}, \tag{31}$$

where the entries in the matrices are obtained by differentiating (18) and (19) ((20) and (21)) with respect to t_k and $\dot{Z}_k$ (t_{k+1} and $\dot{Z}_{k+1}$). The entries of these matrices, as well as the trace $\mathrm{Tr}(DP)$ and determinant $\mathrm{Det}(DP)$ of the matrix DP, are given in Appendix A.2. Using $\mathrm{Tr}(DP)$ and $\mathrm{Det}(DP)$, the eigenvalues of the matrix DP are computed by

$$\lambda_{1,2} = \frac{\mathrm{Tr}(DP) \pm \sqrt{\Delta}}{2}\,, \qquad \Delta = [\mathrm{Tr}(DP)]^2 - 4\cdot\mathrm{Det}(DP)\,,$$

from which we identify parameter ranges of different stable and unstable behavior. If $\Delta < 0$ ($\Delta > 0$), then the eigenvalues $\lambda_{1,2}$ are complex (real), indicating that the fixed point is a focus (node). The stability (instability) of the fixed point corresponds to $|\lambda_j| < 1$ ($|\lambda_j| > 1$) for $j = 1$ or 2. In Figs. 4 and 6, the markers A_1 indicate transitions of the fixed point $\mathbf{H}_k^*$ from stable focus to stable node for decreasing d, while A_2 indicates the change from stable node to stable focus. Point B indicates a period doubling instability, corresponding to the transition from 1:1 periodic solutions to 1:1/2T solutions. We do not show the grazing bifurcation (G) in Fig. 6, restricting our attention to those points obtained by the linear stability analysis. For the case shown in Fig. 6(h), the grazing bifurcation occurs at value of d just slightly above that of B, so that grazing instead of period doubling is observed numerically, as shown in Fig. 4(d),(h).

4. Influence of asymmetric r

In the previous sections we have considered bifurcations and transitions of the solution via the impact velocity $\dot{Z}_k$ as a function of the non-dimensionalized capsule size d. Using the new results from Section 3 we take a different view here, comparing analytical and numerical results for $\dot{Z}_k$ and U_k as r_B and r_T vary. We focus on the ranges where 1:1 and $1{:}1/pT$ periodic solutions are stable, as well as transitions to 2:1 and 1:2 solutions, since these ranges show significant influence on U_k.

4.1. Parameter ranges for key bifurcations

Fig. 7 illustrates the bifurcations from 1:1 periodic solutions as r_B is varied relative to r_T for two different values of inclination angle β. As above, the numerical results are obtained by a continuation-type method, here choosing a value of r_B, computing over a sufficiently long time to reach the attracting behavior shown in terms of $\dot{Z}_k$. This attracting behavior provides the initial condition in the computation for the next value of r_B, typically close to the previous one. We show these results for fixed values of capsule length s and forcing amplitude A, taking $d = .23$. This value is in the range where there are transitions to $1{:}1/pT$ for $r_B \le r_T = .5$, transitions to 2:1 (1:2) solutions for $r_B < r_T$ ($r_B > r_T$), and stable 1:1 behavior for a range of $r_B > r_T$. In order to make comparisons across different choices for r_T, we give results in terms of r_B/r_T.

These figures illustrate how larger β can reduce the range of r_B/r_T over which there are stable 1:1 periodic solutions. This observation is similar to the trend also observed in results for symmetric $r_T = r_B$ in [62,63], namely, that increased β reduces the range of d for stable 1:1 periodic solutions, which lose stability to either $1{:}1/pT$ or 2:1 periodic solutions. The increased angle β introduces additional asymmetry in the behavior, which facilitates period doubling or grazing transitions. For example, increased β can shift the period doubling transition to larger r_B as can be observed from the comparison of panels (a) and (c) in Fig. 7. Taking $r_B \neq r_T$ can result in transitions to either 2:1 or 1:2 depending on r_B/r_T, while the range of d for stable 1:1 solutions also varies with r_B/r_T, as suggested by comparing Figs. 2, 4 and 7. The interplay between d and r_B/r_T is discussed further below. The focus on the stability range of 1:1 solutions is particularly relevant, since proximity to instabilities or bifurcations can limit robust energy output; that is, external perturbations or variation in parameter values can then cause a change in dynamics, which then changes the energy output.

Here we note that $\dot{Z}_k = 0$ corresponding to grazing is not necessarily observed in the numerics shown in Figs. 7 and 8. In some instances the grazing point may lie on an unstable branch of a 2:1 or 1:2 solution with $\dot{Z}_k = 0$, with $\dot{Z}_k \neq 0$ on a stable portion of the branch. Then numerically only the stable portion is observed, as discussed in [63]. In other cases, such as in Fig. 8(c), the continuation method may follow a second solution that is bi-stable with the 2:1 or 1:2 solution, so that the numerically realized transition occurs outside of the bi-stable region, where $\dot{Z}_k \neq 0$.

Within the range of stable 1:1 solutions, we see that there are two different 1:1 solutions. A key difference between these two 1:1 solutions is seen in the transition times Δt_k and Δt_{k+1} for the maps P_1 and P_2, corresponding to the transitions $\partial B \to \partial T$, and $\partial T \to \partial B$, respectively. Recall that $\Delta t_k + \Delta t_{k+1} = T$, so that increasing Δt_k will decrease Δt_{k+1},

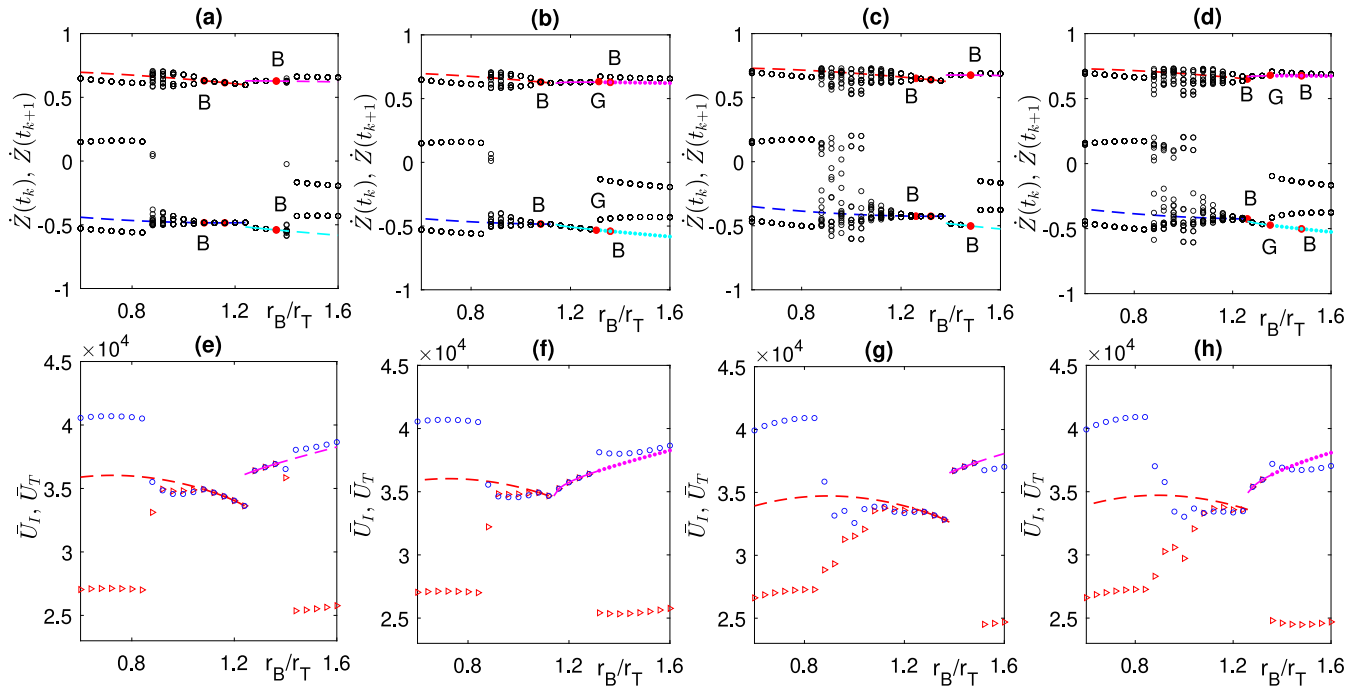

Fig. 7. Bifurcation diagrams and corresponding energy output for changing r_B and fixed $r_T = 0.5$, and $d = .23$, $A = 5$ N, $s = .3695$ m. Top Row: $\dot{Z}_k$ vs. r_B with $\beta = \pi/6$ for (a),(b), and $\beta = \pi/3$ for (c), (d). Points labeled with B and G as described in Section 3.3. Solid (dashed) red and blue lines show relative impact velocity on ∂B and ∂T, respectively, for stable (unstable) $1{:}1_{P_1}$ analytical solutions. Solid (dashed/dotted) magenta and cyan lines show relative impact velocity on ∂B and ∂T, respectively, for stable (unstable via period doubling/grazing) $1{:}1_{P_2}$ analytical solutions. The stable branches are shown only for those values that are also captured numerically, for comparison. (Complete stable branches shown in Fig. 9.) Numerical results shown by black open circles. In (a) and (c), r_B increases, while in (b) and (d) r_B decreases. Bottom Row: Average output voltages per impact, $\overline{U}_I$, and per time interval, $\overline{U}_T$, corresponding to the top row. Numerical results shown by red triangles for $\overline{U}_I$, and blue o's for $\overline{U}_T$. Solid (dashed) line shows average output voltage for the stable (unstable) 1:1 analytical solutions, with $\overline{U}_I = \overline{U}_T$ by definition. Red (magenta) line shows the analytical results $\overline{U}_I, \overline{U}_T$ for $1{:}1_{P_1}$ ($1{:}1_{P_2}$). (For interpretation of the references to color in this figure legend, the reader is referred to the web version of this article.)

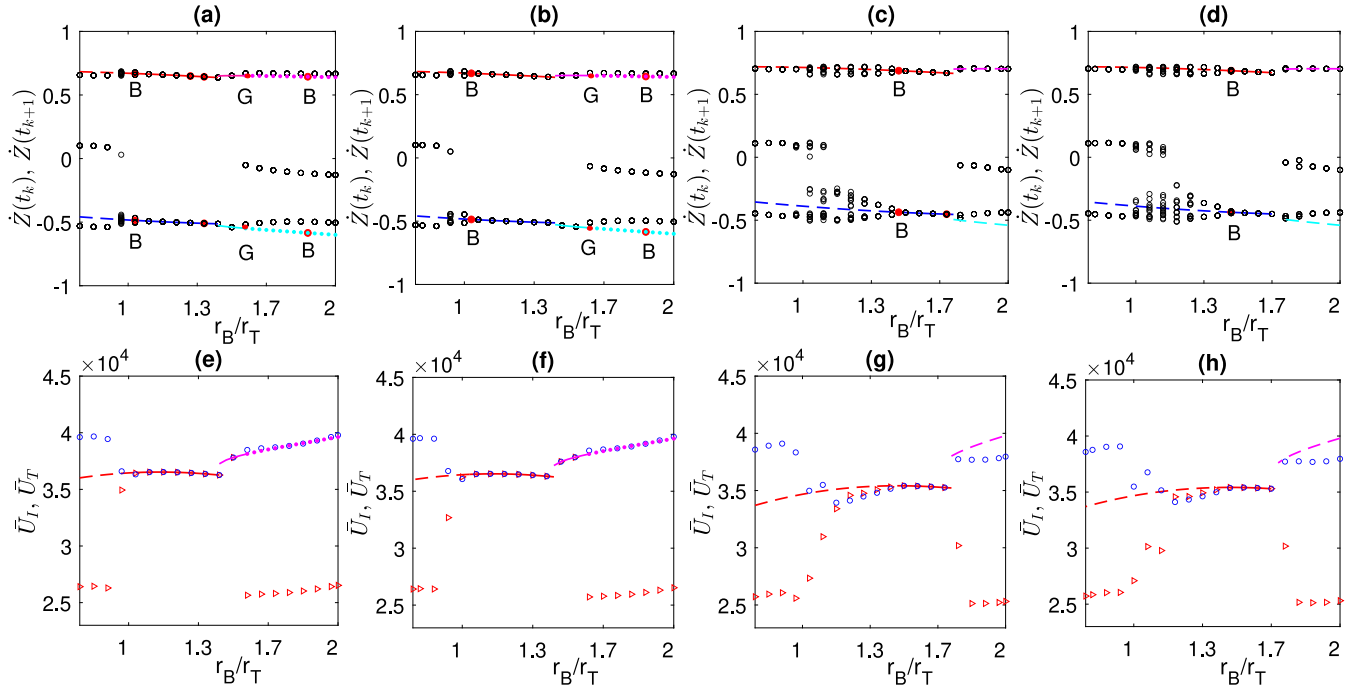

Fig. 8. Bifurcation diagrams and corresponding energy output for changing r_B and fixed $r_T = 0.3$, and $d = .23$, $A = 5$N, Top Row: $\dot{Z}_k$ vs. r_B with $\beta = \pi/6$ for (a), (b), and $\beta = \pi/3$ for (c), (d). Solid (dashed) red and blue lines show relative impact velocity on ∂B and ∂T, respectively, for stable (unstable) $1{:}1_{P_1}$ analytical solutions. Solid (dashed/dotted) magenta and cyan lines show relative impact velocity on ∂B and ∂T, respectively, for stable (unstable via period doubling/grazing) $1{:}1_{P_2}$ analytical solutions. The stable branches are shown only for those values that are also captured numerically, for comparison. Numerical results shown by black open circles. In (a) and (c), r_B increases, while in (b) and (d) r_B decreases. Bottom Row: Average output voltages per impact, $\overline{U}_I$, and per time interval, $\overline{U}_T$, corresponding to the top row. Numerical results shown by red triangles for $\overline{U}_I$, and blue o's for $\overline{U}_T$. Solid (dashed) line shows average output voltage for the stable (unstable) 1:1 analytical solutions, with $\overline{U}_I = \overline{U}_T$ by definition. Red (magenta) line shows the analytical results $\overline{U}_I, \overline{U}_T$ for $1{:}1_{P_1}$ ($1{:}1_{P_2}$). (For interpretation of the references to color in this figure legend, the reader is referred to the web version of this article.)

and vice versa. Incorporating this characterization into the notation, we use the following notation for the different 1:1 solutions,

$$1{:}1_{P_1} : \Delta t_k > T/2 \text{ for } P_1 : \partial B \to \partial T,\ \Delta t_{k+1} < T/2 \text{ for } P_2 : \partial T \to \partial B,$$
$$1{:}1_{P_2} : \Delta t_k < T/2 \text{ for } P_1 : \partial B \to \partial T,\ \Delta t_{k+1} > T/2 \text{ for } P_2 : \partial T \to \partial B. \quad (32)$$

Then $1{:}1_{P_1}$ ($1{:}1_{P_2}$) solutions are observed for smaller (larger) ratios of r_B/r_T, reflecting that larger r_B reduces the time spent in the transition $\partial B \to \partial T$.

Somewhat counter-intuitively, the average output voltage $\overline{U}_I$ for the 1:1 solutions does not change monotonically with increasing r_B, as seen in Figs. 7–8. Rather, $\overline{U}_I$ for $1{:}1_{P_1}$ eventually decreases with increasing r_B, then for larger r_B the stable behavior is $1{:}1_{P_2}$, for which $\overline{U}_I$ is larger and increasing with r_B. In general there is a moderate change in $\overline{U}_I$ and $\overline{U}_T$ at period doubling transitions to $1{:}1/2T$, with more substantial decrease (increase) of $\overline{U}_I$ ($\overline{U}_T$) at the transitions to 2:1 and 1:2 solutions. We observe these abrupt changes in energy output, comparing the values of $\overline{U}_T = \overline{U}_I$ for the $1{:}1_{P_1}$ solutions to the values of $\overline{U}_I$ and $\overline{U}_T$ for the 2:1 solutions. In contrast, in some cases there is a relatively small change in $\overline{U}_T$ at the transition from $1{:}1_{P_2}$ to 1:2 solutions. Of course $\overline{U}_I$ decreases substantially at this transition, due to an additional low velocity impact $\dot{Z}_k \ll 1$ on ∂T. Thus the energy output can vary substantially, as related to the stability of $\dot{Z}_k$ that depends on r_B/r_T.

While panels (a) and (b) in Fig. 7 are generated for the same parameter values, we see that the numerically generated bifurcation branches are different. The difference between (a) and (b) is the direction that the continuation-type method is applied: in (a) it is generated by taking increasing values of r_B, while in (b) r_B is decreasing. By comparing (a) and (b), we conclude that there are regions of bi-stability: that is, one of the two different 1:1 solutions is followed via the continuation method depending on whether r_B is increasing or decreasing: in (a), the $1{:}1_{P_1}$ solution is followed up to a value of r_B with $r_B/r_T > 1.2$ while in (b) the $1{:}1_{P_2}$ solution is followed for a range of r_B with $r_B/r_T < 1.2$. Likewise, comparing (a) and (b), we observe a similar phenomenon at the transition between the 1:1 solution and 1:2 solution for larger r_B: the numerical solution follows the 1:2 solution for a larger range of decreasing r_B, but for increasing r_B the continuation method follows the $1{:}1_{P_2}$ solution for a larger range of r_B. Note that in Fig. 7 we plot with solid lines the analytical results only for those parts of the stable 1:1 branches that are captured by the numerical continuation-type approach, and we show with dashed lines the unstable 1:1 solutions, also obtained analytically, that continue for these branches. Here we focus on the comparison with the numerical results and the energy, and in Section 4.2 we combine these graphs to visualize the bi-stability and discuss the implications for energy output $\overline{U}_I$ and $\overline{U}_T$.

Fig. 8 shows similar comparisons for $r_T = .3$. As might be expected from the results in Fig. 2 for smaller symmetric restitution coefficients, with the smaller value of $r_T = 0.3$, the range of stable 1:1 solutions is shifted to smaller values of r_B and stretched over a larger range of r_B/r_T, particularly for smaller β as in (a) and (b). Likewise the transitions to period doubling and 2:1 and 1:2 periodic motions are shifted to smaller values of r_B. As observed in Fig. 7, and the bifurcation figures of Section 2.3 and Section 3, notable changes in average energy outputs are observed for transitions from 1:1 to 2:1 and 1:2 periodic motions. One difference in Fig. 8 is that the regions of bi-stability for $r_T = .3$ are significantly reduced or removed, as compared with that observed for $r_T = .5$ in Figs. 7 and 9.

4.2. Bi-stability for asymmetric r_T and r_B

The importance of the analytical results is highlighted not only in being able to provide parametric dependence of different types of solutions, but also in identifying and studying regions of bi-stability for the nonlinear dynamics of the VI-EH device. There are a number of instances of bi-stability identified for the symmetric case in [63] and in on-going work [65], indicating generic scenarios where bi-stability is more prevalent for $r_T = r_B$, e.g. for smaller values of β and near transitions to n:1 behavior for $n > 2$. In the case of $r_T \neq r_B$ we can identify additional sources of bi-stability, given that there are different types of 1:1 solutions possible for different combinations of r_T and r_B. Fig. 9 shows this bi-stability, by combining Figs. 7(a) and (b) for $\beta = \pi/6$. This figure shows the analytical results for $\dot{Z}_k$ for the two different branches of 1:1 solutions, with a region of bi-stability located around $r_B/r_T = 1.2$. The values of $\dot{Z}_k$ for these two 1:1 solutions are obtained from the solution of the system (23)–(25), and the (bi-)stability regions for these two solutions are obtained via the linear stability analysis of Section 3.3.

The green circles (black diamonds) in Fig. 9, obtained numerically for increasing (decreasing) r_B are super-imposed on the analytical results for $\dot{Z}_k$, thus illustrating how the numerically generated $\dot{Z}_k$ can miss portions of the locally stable solutions. Specifically, we see that the two numerically generated branches for $\dot{Z}_k$ are similar for smaller values of $r_B/r_T < 1.1$, but in the range $1.1 < r_B/r_T < 1.4$, different 1:1 solutions may be followed depending on the direction of the continuation method, that is, dependent on the initial conditions. For $1.14 < r_B/r_T < 1.26$ the $1{:}1_{P_1}$ and $1{:}1_{P_2}$ solutions are bi-stable, and representative phase planes for these solutions are shown in Fig. 10(c) and (d) for a value in this bi-stability range. Likewise, Fig. 10(a) and (b) show representative phase planes for the bi-stable $1{:}1_{P_2}$ and 1:2 solutions for a value in their bi-stability range, $1.29 < r_B/r_T < 1.37$.

We can see the energy implications of the bi-stability observations by referring to Figs. 9(b). For example, the $1{:}1_{P_2}$ behavior (cyan and magenta branches in Fig. 9(a)) yields larger values of $\overline{U}_I = \overline{U}_T$ (magenta branch in Fig. 9(b)) as compared to $1{:}1_{P_1}$ behavior (red and blue branches in Fig. 9(a)) which yields the red branch of $\overline{U}_I = \overline{U}_T$ in Fig. 9(b). This difference follows directly from the comparison of $\dot{Z}_k$ for these two solutions, with $|\dot{Z}_k|$ larger for the $1{:}1_{P_2}$ solution. Since the 1:2 solution includes an additional impact with $|\dot{Z}_k| \ll 1$ on ∂T, we expect to see differences in $\overline{U}_I$ and $\overline{U}_T$ for the bi-stable $1{:}1_{P_2}$ and 1:2 solutions. Not surprisingly, $\overline{U}_I$ drops by almost a third for the transition from $1{:}1_{P_2}$ to 1:2 behavior. In contrast, the difference for $\overline{U}_T$ is relatively small in the transition between $1{:}1_{P_2}$ and 1:2, as is observed in Fig. 7 for both values of β. These comparisons for $r_T = .5$ show that in these bi-stability regions, for the same parameter values, different output levels of $\overline{U}_I$ and $\overline{U}_T$ can be obtained, depending on initial conditions or equivalently, external perturbations. In contrast, for smaller $r_T = .3$ as shown in Fig. 8, these regions of bi-stability are reduced or removed, as is the dependence of $\overline{U}_I$ and $\overline{U}_T$ on initial conditions or external perturbations.

The comparisons of $\overline{U}_I$ and $\overline{U}_T$ in the bi-stability ranges raise a number of questions. Given different initial conditions, which of the bi-stable behaviors is more likely, and what are the implications for energy output? Mathematically, this is essentially a question about the basins of attraction for these different behaviors, given all possible initial conditions or perturbations. While we leave this question for future work, we note that the explicit analytical solution $(\dot{Z}_k, \varphi_k, \Delta_k)$ and the maps used to construct it form a valuable basis from which to explore these larger questions. Furthermore, the shape of the solutions in the phase plane as shown in 10, as well as the change in the phase at impact φ_k as shown in Fig. 5, suggest other future directions for exploring the transitions between bi-stable solutions.

4.3. Transition boundaries in parameter space

Figs. 7–8 give results for a fixed value of d, chosen somewhat arbitrarily for its proximity to different types of bifurcations as shown in Figs. 2 and 4. Parametrically, one is interested in the location of these transitions for a range of d. Given that 1:1 periodic behavior tends to yield larger $\overline{U}_I$, and that $\overline{U}_T$ increases with transitions to 2:1 and 1:2 solutions, we pay careful attention to the regions for stable 1:1 motions and to transitions to period doubling as well as to 1:2 and 2:1 behavior.

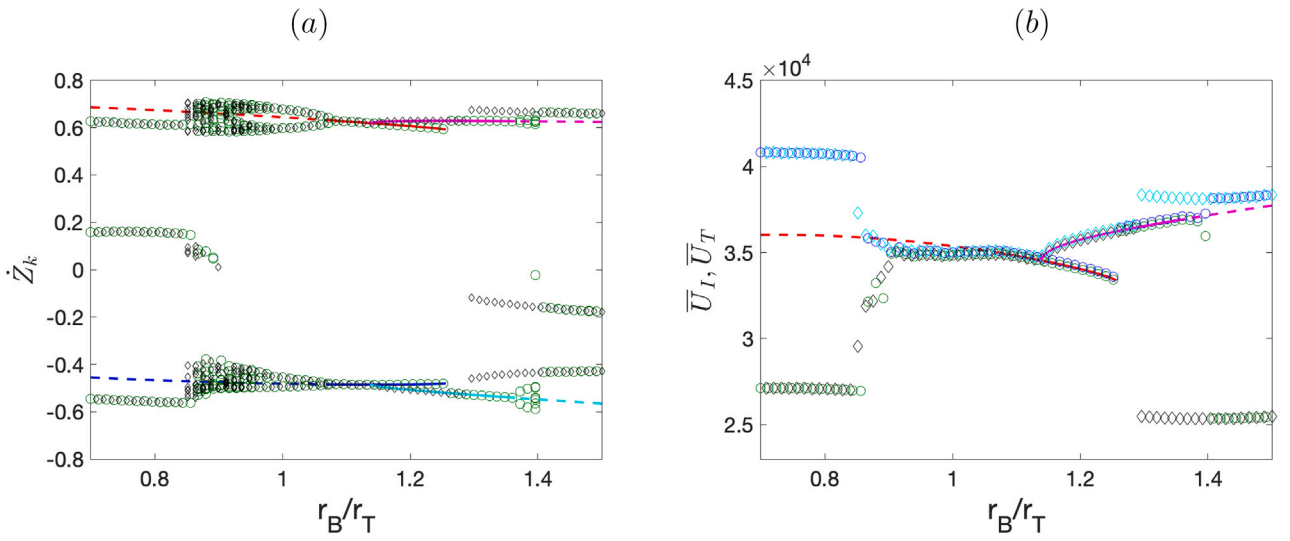

Fig. 9. Left: Combined bifurcation figures from Fig. 7(a) and (b) showing bi-stability of $1{:}1_{P_1}$ and $1{:}1_{P_2}$ solutions, and bi-stability of $1{:}1_{P_2}$ and 1:2 solutions over a range of r_B. The green circles (black diamonds) obtained numerically via the continuation-like method for increasing (decreasing) r_B. Solid (dashed) red and blue lines show relative impact velocity on ∂B and ∂T, respectively, for stable (unstable) $1{:}1_{P_1}$ analytical solutions. Solid (dashed) magenta and cyan lines show relative impact velocity on ∂B and ∂T, respectively, for stable (unstable via period doubling/grazing) $1{:}1_{P_2}$ analytical solutions. Right: Average energy outputs $\overline{U}_I$, and $\overline{U}_T$ for the branches shown in the left panel. Solid (dashed) red and magenta lines correspond to $1{:}1_{P_1}$ and $1{:}1_{P_2}$, respectively, stable (unstable) branches, where $\overline{U}_I = \overline{U}_T$ for these periodic solutions. Green circles (black diamonds) give $\overline{U}_I$ for increasing (decreasing) r_B. Blue circles (cyan diamonds) give $\overline{U}_T$ for increasing (decreasing) r_B. (For interpretation of the references to color in this figure legend, the reader is referred to the web version of this article.)

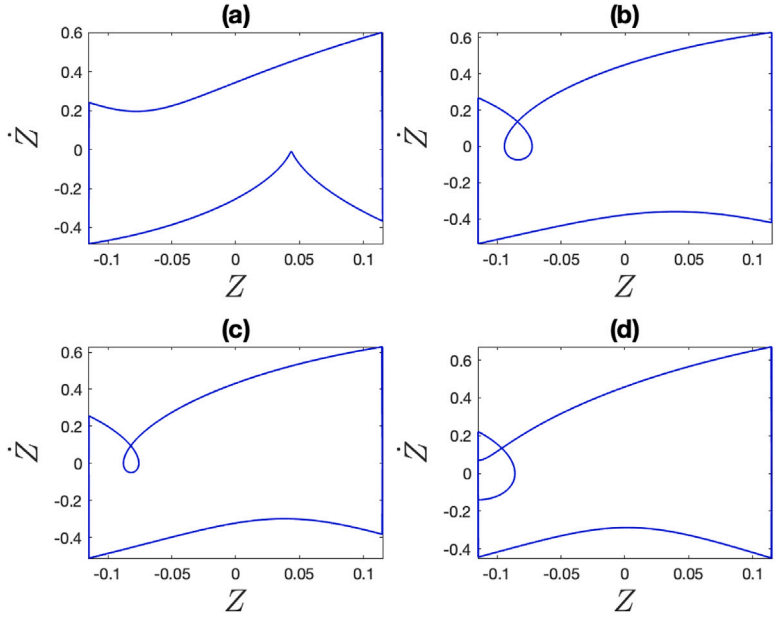

Fig. 10. Phase plane for solutions corresponding to two bi-stable solutions at $r_B/r_T = 1.22$, $1{:}1_{P_1}$ (a) and $1{:}1_{P_2}$ (c); and two bi-stable solutions at $r_B/r_T = 1.34$, $1{:}1_{P_2}$ (b) and 1:2(d).

Figs. 11–12 show the transitions in the VI-EH behavior, in the combined parameter space of the $r_B - d$ plane for fixed r_T and β. By super-imposing these different transitions over the heat map of $\overline{U}_I$ and $\overline{U}_T$, we are able to observe the different state transitions in terms of the ratio r_B/r_T and d, and their impact on the average energy outputs $\overline{U}_I$ and $\overline{U}_T$. In both figures the numerical results are obtained for decreasing d via continuation-type methods as described in Section 2.3, with s decreasing in Fig. 11 and A increasing in Fig. 12. The results indicate parameter regions for which the 1:1 solution is stable, regions of period doubling, leading to more complex solutions particularly for larger β, and regions where grazing generates asymmetric n:1 or 1:n solutions which typically have lower $\overline{U}_I$ and increased $\overline{U}_T$.

In the Figures we indicate the 1:1 to 1:1/2T period doubling via red $*$, obtained via the analysis given in Sections 3.1 and 3.3 . As d decreases further, there may be additional period doublings, as observed in the bifurcation figures above, but we do not show them here. Following a sequence of period doubling bifurcations, eventually a 1:2 or 2:1 solution is reached, with this transition indicated by black diamonds in Figs. 7–8. For some parameters, grazing occurs for larger d than for the period doubling transition, yielding a direct transition from 1:1 to either 2:1 or 1:2 behavior also indicated by black diamonds. In this case the period doubling of the 1:1 solution can still be calculated analytically, even though not observed numerically, indicated with smaller red o's. Note that this period doubling transition

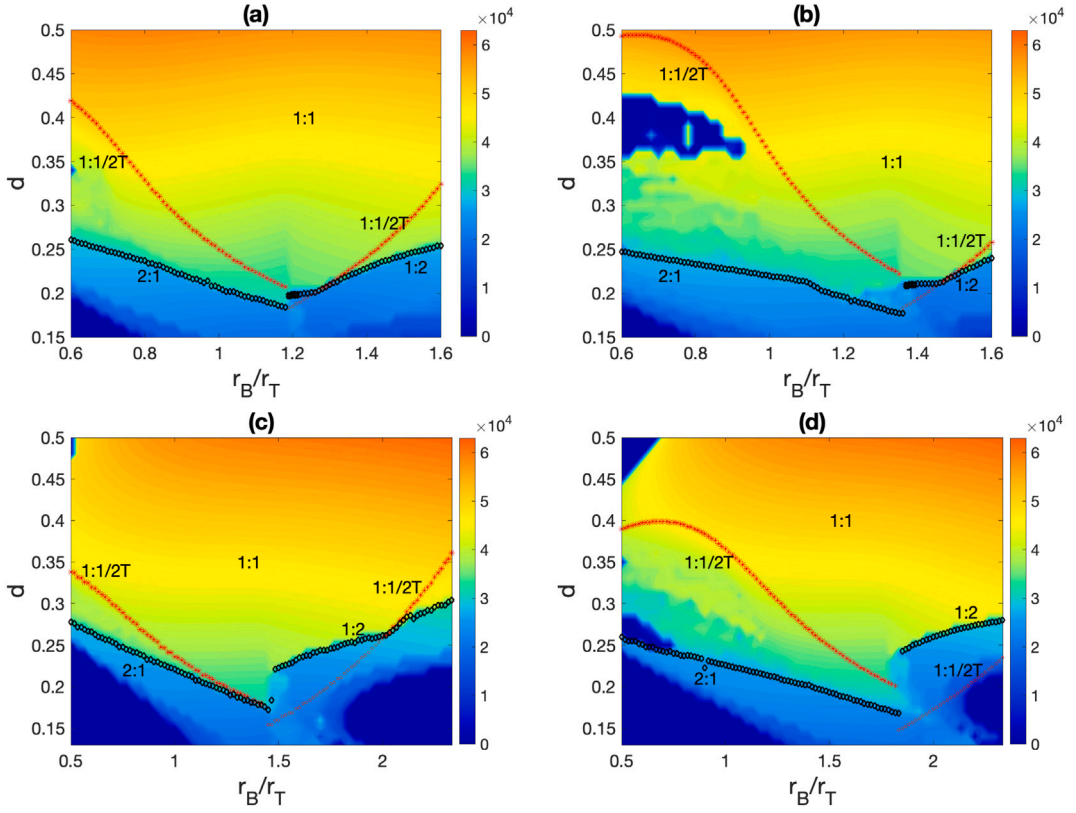

Fig. 11. Superposition of period doubling and grazing bifurcations on heat map of $\overline{U}_I$. Red ∗'s and o's give transitions to 1:1/2T obtained analytically in Section 3.3. Black open diamonds show transitions to 2:1 and 1:2 solutions, obtained via the continuation-type method for fixed r_B and decreasing s. Solid black diamonds indicate transitions to n:1 behavior for $n > 2$. For all graphs $A = 5$ N, with $r_T = .5$ (top) and $r_T = .3$ (bottom); $\beta = \pi/6$ (left), $\beta = \pi/2$ (right). Larger red ∗'s correspond to transitions also observed in simulations, while smaller red o's correspond to analytical results for 1:1/2T, not observed numerically. For those values 2:1 or 1:2 motion via grazing preempts period doubling. (For interpretation of the references to color in this figure legend, the reader is referred to the web version of this article.)

is not observed in the dynamics, given that the grazing transition to 2:1 or 1:2 behavior changes the character of the solution, thus preempting the period doubling transition to 1:1/2T behavior. Since the grazing transition to 1:2 or 2:1 behavior is related to the impact condition, rather than to eigenvalues as in the linear stability analysis of Section 3.3, the grazing transitions are determined independently by tracking the impact velocities. We note that the transitions from 1:1 to 2:1 or 1:2 solutions can also be obtained analytically following the procedure in [65], but we do not pursue that here.

The comparisons in Figs. 11–12 for different combinations of $r_T = .5$ and $r_T = .3$ and smaller and larger β indicate common trends and important differences for the dynamics and the resulting $\overline{U}_I$ and $\overline{U}_T$. As could be expected from the bifurcation plots above, the range of r_B with stable 1:1 behavior increases with d, regardless of inclination angle. Furthermore, $|\dot{Z}_k|$ decreases with decreasing s, and increases with increasing A, and accordingly we see the trend of decreasing or increasing $\overline{U}_I$ and $\overline{U}_T$ in the figures. As noted in Section 4.1, there are two different 1:1 solutions for $r_T \neq r_B$. With results obtained via the continuation-type method, fixing r_B and decreasing d, the results suggest a value of r_B, denoted here as $r_B^{1:1}$, that delineates the regions where the different 1:1 behaviors are observed. Specifically, $1{:}1_{P_1}$ is observed for $r_B < r_B^{1:1}$ and $1{:}1_{P_2}$ for $r_B > r_B^{1:1}$. For this particular continuation computation, this value is suggested by the abrupt changes in dynamical behavior and corresponding $\overline{U}_I$ and $\overline{U}_T$. We then use $r_B^{1:1}$ to discuss these abrupt changes below, with one caution. Based on the bi-stability results discussed in Section 4.2, this cut-off between 1:1 behaviors is not necessarily a single value of r_B. As shown in Fig. 9, there may be bi-stable regions near the transitions between different 1:1 behavior and 1:1 and 1:2 dynamics. Then, depending on initial conditions, external perturbations, or fluctuations in parameters, in these regions of bi-stability there can be additional transitions or hysteresis in the observed $\overline{U}_I$ and $\overline{U}_T$ as r_B varies. Therefore our references to $r_B^{1:1}$ should be interpreted to be a value within a possible band of bi-stability, in which abrupt changes in $\dot{Z}_k$ and corresponding $\overline{U}_I$ and $\overline{U}_T$ can be observed.

While we use $r_B^{1:1}$ to indicate the transition between different 1:1 solutions, it is also related to the transition to 2:1 or 1:2 solutions indicated by the black diamonds in Figs. 11–12. This follows intuitively from the definition of $1{:}1_{P_1}$ and $1{:}1_{P_2}$ in (32). Given the differences in $\overline{U}_I$ and $\overline{U}_T$ observed in transitions from 1:1 behavior and 1:2 and 2:1 solutions, $r_B^{1:1}$ is an important factor in energy output. Recall that $r_B < r_B^{1:1}$ indicates reductions in $\dot{Z}_k$ on the bottom membrane, so that $1{:}1_{P_1}$ spends a longer time in $P_1 : \partial B \to \partial T$ with $\Delta t_k > \Delta t_{k+1}$. This behavior is illustrated in Fig. 10(a), with the trajectory in the P_1 map naturally leading to the 2:1 behavior as d decreases. Similarly, for $r_B > r_B^{1:1}$, the periodic $1{:}1_{P_2}$ solution spends more time in $P_2 : \partial T \to \partial B$ (Fig. 10(b),(c)). Then for smaller d, the trajectory in the P_2 map leads to 1:2 behavior (Fig. 10(d)).

The sequence of bifurcations observed for decreasing d is also different on either side of $r_B^{1:1}$, as shown in Figs. 11–12. Likewise different sequences of $\overline{U}_I$ and $\overline{U}_T$ for decreasing d are observed. Transitions through period doubling can lead to more complex or chaotic behavior, characterized by regions with complex transitions in $\overline{U}_I$ or $\overline{U}_T$. In contrast, transitions via grazing to 2:1 or 1:2 behavior yields sharp transitions in $\overline{U}_I$ (decreasing) or $\overline{U}_T$ (increasing). Specifically, as d decreases with s, the $1{:}1_{P_1}$ solution typically undergoes period doubling transitions and then 2:1 behavior, rather than a grazing transition directly to 2:1 behavior. In contrast, the $1{:}1_{P_2}$ solution transitions directly to either period doubling or 1:2 behavior via grazing, depending on the combination of β, r_T and r_B. As d decreases with increasing A, we see that either of the 1:1 solutions may undergo grazing, thus transitioning

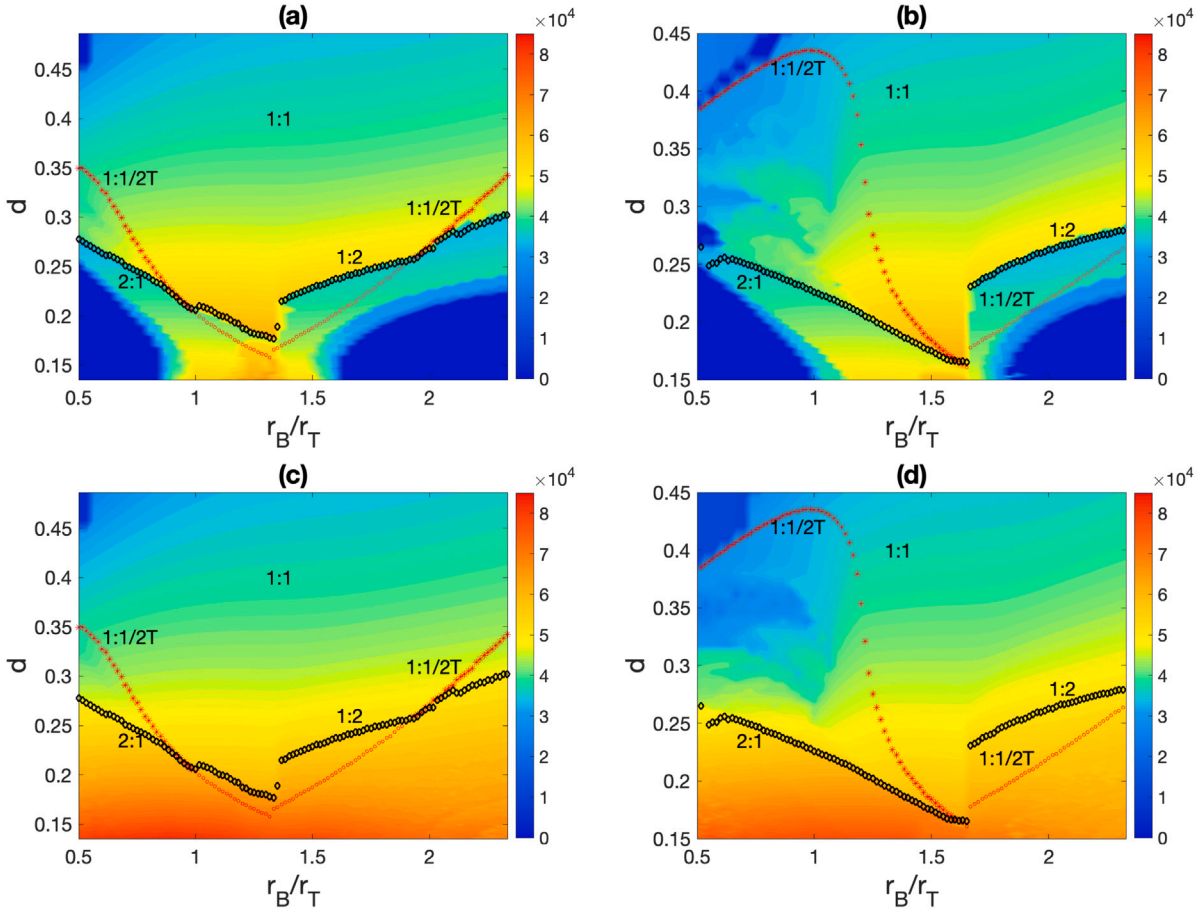

Fig. 12. Superposition of period doubling and grazing bifurcations on heat maps of $\overline{U}_I$ (top row) $\overline{U}_T$ (bottom row). Red $*$'s and o's give transitions to $1{:}1/2T$ obtained analytically in Section 3.3). Black open diamonds show transitions to 2:1 and 1:2 solutions, obtained via the continuation-type method for fixed r_B and decreasing d via increasing A (and decreasing $\bar{g}$). Period doubling indicated by o's not observed numerically, since 2:1 or 1:2 occur first for decreasing d. In (a)–(d) $r_T = .3$, $\beta = \pi/6$ (left), $\beta = \pi/2$ (right). (For interpretation of the references to color in this figure legend, the reader is referred to the web version of this article.)

to 2:1 or 1:2, particularly for r_B closer to $r_B^{1:1}$. In general the transition to 1:2 behavior for $r_B > r_B^{1:1}$ occurs for larger d than for the 2:1 transition for $r_B < r_B^{1:1}$. The period doubling transition of $1{:}1_{P_1}$ is shifted to smaller d for r_B near $r_B^{1:1}$, and for smaller r_T the transition to 2:1 precedes period doubling in this region (Fig. 12(a), (c)).

As would be expected from $\overline{U}_I$ or $\overline{U}_T$ shown in Figs. 7 and 8, the presence of two different 1:1 solutions contributes to their non-monotonic dependence on r_B. In the region with stable 1:1 behaviors the change in $\overline{U}_I = \overline{U}_T$ at $r_B^{1:1}$ is noticeable for values of d just above the 2:1 and 1:2 transition curves. Furthermore, it is obvious from the heat map for $\overline{U}_I$ and $\overline{U}_T$ for values of d below these curves, (e.g. see Fig. 11(a)–(b)). In addition to the energy difference associated with the different 1:1 solutions and the 1:2 or 2:1 transitions, for $r_B \lesssim r_B^{1:1}$ we find the largest range of d for stable 1:1 solutions, specifically for $1{:}1_{P_1}$. (There are some exceptions for combinations of small r_B, r_T, and β values (not shown), as studied in ongoing work [65]). For fixed d, larger energy outputs are often found near $r_B^{1:1}$, although that is not true for all r_T. As observed in Figs. 2, 4 and 7, the transitions to 2:1 or 1:2 behavior yield sharp decreases in $\overline{U}_I$. While in general the period doubling transitions to $1{:}1/2T$ do not yield a sharp increase or decrease in energy output, it can lead to complex behaviors with smaller $\dot{Z}_k$ and lower U_k, typically not robust to perturbations or parameter fluctuations. For larger β and $r_B < r_T$, the increased influence of gravity yields a sequence of period doublings following the $1{:}1_{P_1}$ to $1{:}1/2T$ transition, resulting in large regions of complex behavior with low $\overline{U}_I$ (isolated blue regions in the heat maps), as well as irregular trends in $\overline{U}_T$. In contrast, for larger β and smaller r_T, the $1{:}1_{P_2}$ solution tends to reach the 1:2 grazing transition before any period doubling. Then for larger β, the $1{:}1_{P_2}$ is stable over a larger range of d than the $1{:}1_{P_1}$ solution is, except near $r_B = r_B^{1:1}$. This larger range of stability allows a larger range of operation where the dynamics and energy output is robust to fluctuations or external perturbations.

A comparison of Figs. 11–12 illustrates how one may wish to tune values of r_T and r_B based on different preferences for the impact dynamics and the energy output, as well as for potential wear in the device. With a focus on $\overline{U}_I$, we observe some general trends across all panels. Prioritizing on $\overline{U}_I$ corresponds to a choice of behavior with symmetric wear and tear. That is, the output is best for regular 1:1 behavior, or in the case of smaller d, for 1: n behavior for smaller values of n. For smaller d, there is an advantage to operate at values of r_B just below $r_B^{1:1}$, while avoiding $r_B \geq r_B^{1:1}$ that can lead to 1:2 behavior with smaller $\overline{U}_I$. For larger d there is an advantage to operate at $r_B > r_B^{1:1}$, away from 1:2 grazing bifurcation. In contrast, if the goal is to maximize $\overline{U}_T$, a different behavior may be preferred. For example, for smaller d the largest value of $\overline{U}_T$ is found in periodic n:1 solutions appearing below the transition to 2:1 behavior. Here n may be large, as long as it does not approach sticking behavior where the ball follows ∂B most of the time. This n:1 behavior can cause asymmetric wear, given significantly more impacts on one end. For larger d, $\overline{U}_T$ is maximized by taking r_B as large as possible, corresponding to either 1:2 or $1{:}1_{P_2}$ behavior. Whether the preference is to maximize $\overline{U}_I$ or $\overline{U}_T$, it is achieved generically with $r_B \neq r_T$.

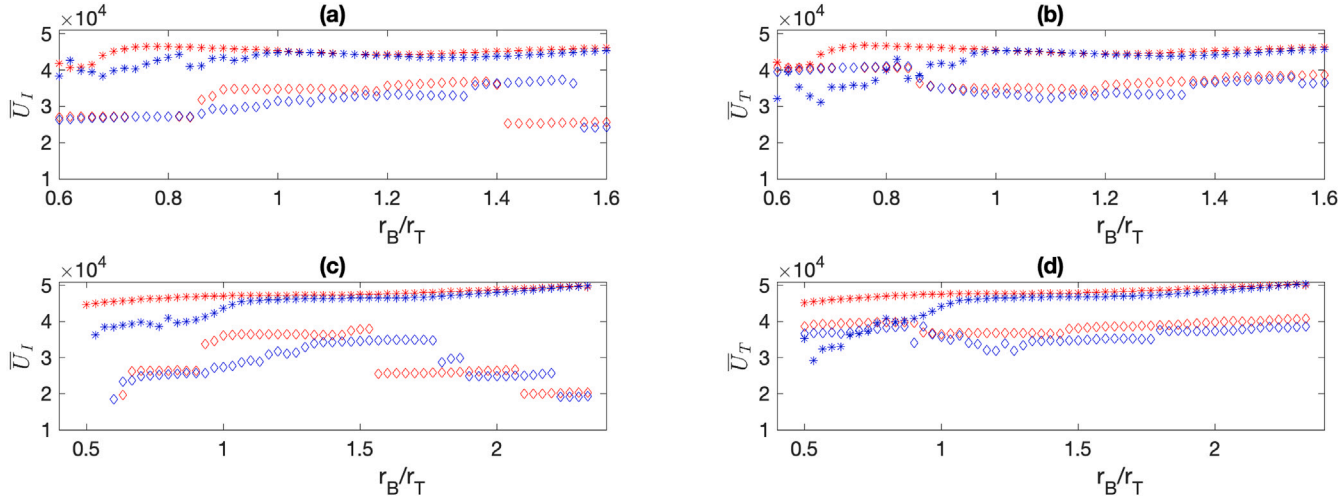

Fig. 13. Comparison of $\overline{U}_I$ (left) and $\overline{U}_T$ (right) as shown in Fig. 11, at $d = .23$ (diamonds) and $d = .35$ (∗), for $\beta = \pi/6$ (red) and $\beta = \pi/2$ (blue). Top row is $r_T = .5$, Bottom row is $r_T = .3$. (For interpretation of the references to color in this figure legend, the reader is referred to the web version of this article.)

4.4. Asymmetric r counteracting other factors

In Fig. 13 we compare the average energy output $\overline{U}_I$ (left) and $\overline{U}_T$ (right) at two different values of d, for different r_T and β, over a range of r_B/r_T. Each set of markers corresponds to taking a horizontal sample at a specific value of d from one of the panels in Figs. 11. Then this figure compares the energy levels for $\overline{U}_I$ across different panels in Fig. 11 and likewise for $\overline{U}_T$. Not surprisingly the energy output is approximately the same for the 1:1 behavior with two different incline angles, $\beta = \pi/6$ and $\beta = \pi/2$, given the similarities in impact velocities. The clearest differences in energy output due to β are related to the transitions to 2:1 and 1:2 behavior. For $r_T = 0.3$ and $d = 0.23$ there are a series of transitions to n:1 and 1:n behavior, which appear as a series of steps in the level of $\overline{U}_I$. These steps are shifted to larger or smaller r_B depending on β. In contrast, the transition from $1{:}1_{P_2}$ to 1:2 behavior, for larger r_B, does not result in a large increase or drop in $\overline{U}_T$, as previously observed from Fig. 7. However, $\overline{U}_T$ is reduced for complex solutions for smaller r_B following a sequence of period doublings (isolated blue regions in Figs. 11–12), not studied in detail in this paper. In either case, the steps or variations in $\overline{U}_I$ or $\overline{U}_T$ indicate that energy output is generically not robust near these bifurcations, since the dynamics tends to be qualitatively sensitive to parametric fluctuations or external perturbations. As discussed above for Figs. 11 and 12, we again note that the maximum energy output in general does not occur for the previously studied symmetric case $r_T = r_B$.

These energy comparisons across different parameters raise the question: Can asymmetry in restitution coefficients be introduced to counteract detrimental effects from asymmetry due to the angle β? Then changing r_T or r_B facilitates shifting to different states as mapped out in Figs. 11 and 12.

In particular, the comparisons above in Fig. 13 and in previous bifurcation figures show that increased β can drive period doubling and grazing bifurcations. Furthermore, the range of stable 1:1 solutions shifts for r_B and r_T, suggesting that changes in the restitution coefficient can result in 1:1 solutions similar to those seen for smaller β. Fig. 14(a) and (d) illustrate cases where larger β results in irregular behavior with lower energy output. The complex (chaotic) behavior observed for $\beta = \pi/2$ in panel (a) corresponds to the behavior seen after a sequence of period doublings. With decreased r_T as in (c), the dynamics shifts to 1:1 behavior that is similar to the 1:1 behavior observed for smaller $\beta = \pi/6$ and larger r_T in (b). Panels (d)–(f) give an example for larger $d = 0.3$, with a complex, low energy state shown for $\beta = \pi/2$ in (d), as also observed in Fig. 11(b). The behavior shifts to stable 1:1 behavior for increasing r_B (f), similar to the 1:1 behavior obtained for smaller angle $\beta = \pi/6$ in (e). Both examples shown in (a)–(c) and (d)–(f) indicate how changes in asymmetric r_T and r_B can change the behavior from complex dynamics with low energy output to a stable 1:1 with larger energy output. The asymmetric choice takes advantage of the larger stability regions of 1:1 behavior for certain combinations of r_T and r_B.

The benefit of changing r_T or r_B is not limited to cases where β is larger. Fig. 13(g)–(i) shows a case where a smaller $\beta = \pi/6$ yields a lower energy solution (g), due to a 1:2 bifurcation as observed for larger values of r_B/r_T in Figs. 7–8. Then decreasing r_B yields a 1:1 solution in panel (i), similar to increasing the angle to $\beta = \pi/3$ (h).

5. Conclusions

For a model of a two-sided vibro-impact energy harvester, we study the influence of asymmetric restitution coefficients on periodic solutions, and the implications for the device's energy output. An impact pair forms the basis of the model, in which a ball moves freely within a forced cylinder and collides on either end against a flexible dielectric polymer with compliant electrodes, thus converting the motion into output voltage. We develop (semi-)analytical results for 1:1 periodic solutions and their stability. The analysis is based on maps that encode the dynamics between impacts to provide conditions for stable 1:1 periodic solutions in terms of the system parameters. These solutions are given in terms of three key characteristics of the solutions, the impact velocity at the kth impact, $\dot{Z}_k$, the phase shift φ_k of the impact relative to the forcing, and the length of time Δt_k that the ball spends traversing the length of the cylinder following the kth impact. The advantage of this analysis is that it captures the parametric dependence for the dynamical behavior, thus indicating the benefits and disadvantages of operating in certain parameter regimes.

With asymmetric restitution coefficients r_T and r_B, on the top and bottom of the cylinder, respectively, there are new types of 1:1 periodic solutions that are possible, not observed in the symmetric case $r_T = r_B$. Specifically, for $\beta > 0$ and $r_T = r_B$, the 1:1 periodic solutions spend more time in transition from bottom to top than from top to bottom, which is expected due to the gravity. However, for certain $r_B/r_T > 1$ it is possible to have 1:1 periodic solutions that spend more time in transition from top to bottom than from bottom to top. This new type of 1:1 behavior can generate larger energy output. The transition between the different 1:1 solutions, through varying r_B/r_T, has other implications for the dynamics and the energy output. The energy output varies non-monotonically, specifically near the transition between 1:1 solutions, which suggests some parameter ranges with

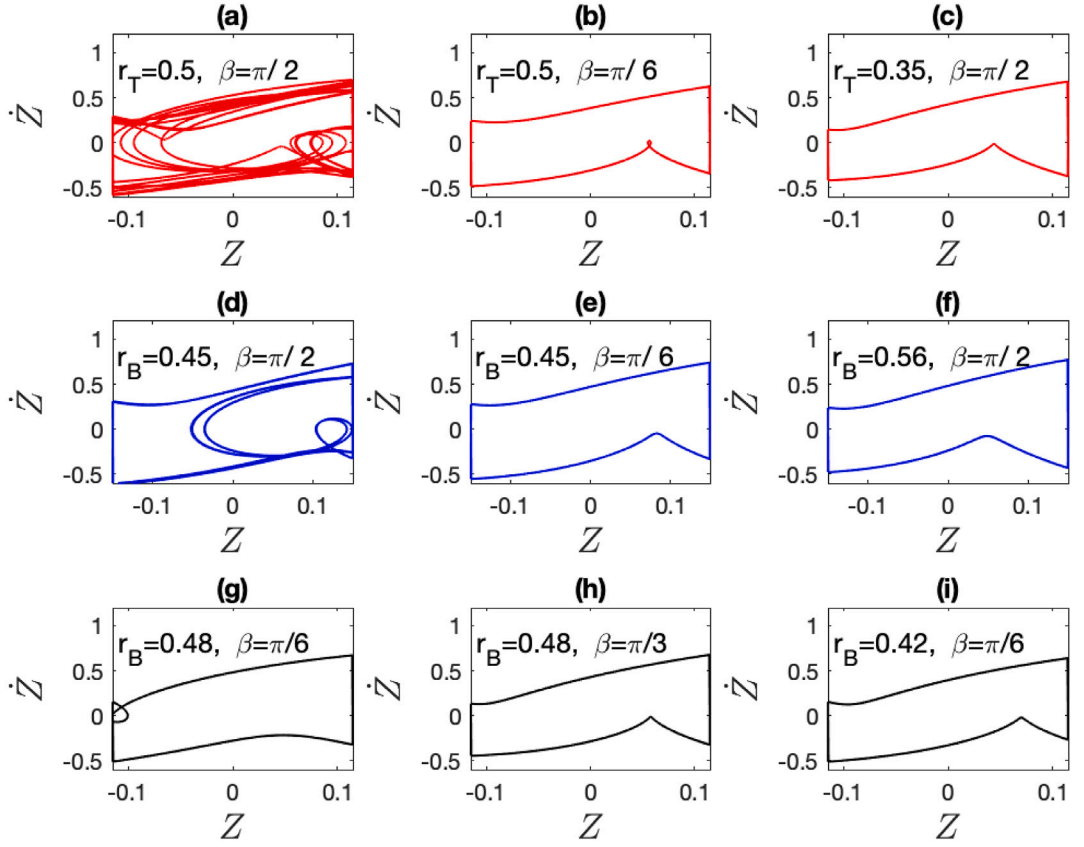

Fig. 14. Three examples where a change in r_T or r_B shifts the dynamics to 1:1 behavior, similar to that seen for a change in β. Top row (red): $r_B = .55$, $d = .23$; Middle row: $r_T = .5$, $d = .3$; Bottom row (black): $r_T = .3$, $d = .23$. In all panels $A = 5$ N. (For interpretation of the references to color in this figure legend, the reader is referred to the web version of this article.)

better performance. Near this transition there are larger parameter ranges for stable 1:1 behavior, which is preferable for larger average energy per impact and symmetric wear in the device.

There are a number of non-intuitive results that appear with $r_T \neq r_B$. For example, a smaller restitution coefficient can generate a larger energy output, even though the coefficient leads to a reduced relative velocity immediately following the impact. In this case we see the influence of the asymmetry on other important characteristics of the behavior, specifically on φ_k. This phase shift can drive a net gain of the impact velocities over the forcing period, and thus improve the level of the energy output. The asymmetry can also improve the robustness of the regular behavior, via an extension of its stability range, thus reducing susceptibility to perturbations or chaotic behavior which can reduce the energy output. Furthermore, the analytical results provide bi-stability ranges of the different 1:1 solutions that may be missed from numerical calculations, depending on the method that is used. Since there is a difference in the energy output for these different bi-stable solutions, one would prefer to operate with the dynamics that produces more energy.

The analytical solutions are compared to numerically generated bifurcations that give the critical transitions between 1:1 periodic solutions and other more complex behaviors, via period doubling or grazing bifurcations. The difference in the time between impacts also has implications for the type of solution that can occur via grazing. Grazing can occur with increased asymmetry in the restitution coefficients, increased inclination angle β, or reduced non-dimensional cylinder length. Complementary to grazing bifurcations to 2:1 solutions that are observed for $r_T = r_B$, with larger r_B/r_T there are bifurcations to 1:2 solutions, with an additional small velocity impact per period on the top of the cylinder. Depending on the priorities for energy output, average energy per time interval or per impact, it may or may not be beneficial to operate in this range. There are several types of n:1 and 1:n solutions observed numerically, which obviously contribute more energy per time interval, but can be responsible for increased wear with more impacts per period occurring asymmetrically.

As we compare the different types of periodic solutions with energy output, we identify several detrimental parameter combinations that contribute to asymmetry and may reduce the level of output. These usually occur in terms of increased inclination angle and larger asymmetries in restitution coefficients. By understanding how the asymmetric restitution coefficients can contribute to bifurcations and complexity, we are able to propose adjustments to the asymmetric restitution coefficients that may counteract negative effects of inclination angle (or of other parameters). Beyond these results, the analysis and comparisons with computations indicate a rich variety of dynamical behaviors with direct relevance to energy output, such as bi-stability, hysteresis, and robustness to transitions driven by stochastic perturbations, which we defer for future in-depth study.

Based on the analysis and comparison with computations in this paper, we summarize the applied engineering recommendations and conclusions:

- Reducing the restitution coefficient may improve the level and/or robustness of energy output, which is directly related to phase differences between impacts and external forcing
- Asymmetry in the restitution coefficients can extend the range of beneficial periodic solution, when correctly selected, but it can also introduce asymmetric and complex motions with potential bi-stability.
- Depending on the value of the system's parameters the absolute maximum power output can be achieved at asymmetric values of the restitution coefficient. Moreover, for a small value of the

inclination angle β, the maximum will be reached when $r_B/r_T < 1$, whereas for a large value of β it is observed for $r_B/r_T > 1$.

CRediT authorship contribution statement

Sam Dulin: Methodology, Software, Writing – original draft, Writing – review & editing. **Kailee Lin:** Software, Writing – review & editing. **Larissa Serdukova:** Methodology, Software, Writing – original draft, Writing – review & editing. **Rachel Kuske:** Conceptualization, Methodology, Software, Validation, Writing – review & editing. **Daniil Yurchenko:** Conceptualization, Methodology, Validation, Writing – review & editing.

Declaration of competing interest

The authors declare that they have no known competing financial interests or personal relationships that could have appeared to influence the work reported in this paper.

Acknowledgments

The authors gratefully acknowledge partial funding for this work from NSF-CMMI 2009270 and EPSRC EP/V034391/1.

Appendix

A.1. Analytical approximation of 1:1 periodic solution

We demonstrate the steps for an alternate system of equations to (23)–(25) for $\dot{Z}_k$ and φ in terms of q. These are shown for the specific choice, $f(t) = \cos(\pi t + \varphi)$ which allows further reductions of the system. 3. First we combine Eqs. (18)–(20) and use the periodic conditions (22) to get

$$\dot{Z}_{k+1} + \dot{Z}_k = -r_B\dot{Z}_k - r_T\dot{Z}_{k+1} + \bar{g}T \implies \dot{Z}_{k+1} = \frac{\bar{g}T}{1+r_T} + \zeta\dot{Z}_k \tag{33}$$

where $\zeta = -\frac{1+r_B}{1+r_T}$. Next, we substitute (33) into (18) to get

$$F_1(t_{k+1}) - F_1(t_k) = (\zeta + r_B)\dot{Z}_k + \bar{g}\left(\frac{T}{1+r_T} - T_1\right). \tag{34}$$

Then we derive an expression for $\dot{Z}_k$ dependent only upon quantities at impact time t_k by adding Eqs. (19) and (21), using the periodic conditions, and substituting in (33) and (34):

$$\begin{aligned}
0 = &-r_B\dot{Z}_kT_1 - r_TT_2\left(\frac{\bar{g}T}{1+r_T} + \zeta\dot{Z}_k\right) + \frac{\bar{g}}{2}(T_1^2+T_2^2) - F_1(t_k)T - \\
&- T_2\left[(\zeta+r_B)\dot{Z}_k + \bar{g}\left(\frac{T}{1+r_T} - T_1\right)\right] \implies \\
F_1(t_k) = &\frac{1}{T}\cdot\left[\lambda\dot{Z}_k - r_TT_2\frac{\bar{g}T}{1+r_T} + \frac{\bar{g}}{2}(T_1^2+T_2^2) - T_2\frac{\bar{g}T}{1+r_T} + \bar{g}T_1T_2\right] \implies \\
F_1(t_k) = &\frac{1}{T}\cdot\left[\lambda\dot{Z}_k - \bar{g}TT_2 + \frac{\bar{g}}{2}(T_1^2+T_2^2) + \bar{g}T_1T_2\right].
\end{aligned} \tag{35}$$

with $\lambda = [-r_BT_1 - r_T\zeta T_2 - T_2(\zeta + r_B)]$. Now we combine Eqs. (35) with (19) to obtain

$$\begin{aligned}
F_2(t_{k+1}) - F_2(t_k) = &-d + \dot{Z}_k\left(r_BT_1 + \frac{\lambda T_1}{T}\right) - \frac{\bar{g}}{2}T_1^2 - \bar{g}T_1T_2 + \frac{\bar{g}T_1^2T_2}{T} + \\
&+ \frac{\bar{g}T_1}{2T}(T_1^2+T_2^2).
\end{aligned} \tag{36}$$

Finally, to get an equation for $\dot{Z}_k$ in terms of q only, we square (34) and (36) and add them

$$\begin{aligned}
&[F_2(t_{k+1}) - F_2(t_k)]^2 + [F_1(t_{k+1}) - F_1(t_k)]^2 = \\
&= \left[-d + \dot{Z}_k\left(r_BT_1 + \frac{\lambda T_1}{T}\right) - \frac{\bar{g}}{2}T_1^2 - \bar{g}T_1T_2 + \frac{\bar{g}T_1^2T_2}{T} + \frac{\bar{g}T_1}{2T}(T_1^2+T_2^2)\right]^2 + \\
&+ \left[(\zeta+r_B)\dot{Z}_k + \bar{g}\left(\frac{T}{1+r_T} - T_1\right)\right]^2.
\end{aligned} \tag{37}$$

The resulting simplifications of (34), (35), and (38) for the specific sinusoidal forcing $f(t)$ are shown in Section 3. For example, (38) reduces to a quadratic equation for $\dot{Z}_k$, with coefficients a, b, and c given by

$$a = \pi^2(\zeta + r_B)^2 + \pi^4 q(\lambda + 2r_B), \tag{39}$$

$$b = 2q\pi^4(\lambda + 2r_B)(2\bar{g}q^2 - 2\bar{g}q - d) - \frac{4\bar{g}\pi^2}{r_T+1}(r_B+\zeta)(q + r_Tq - 1), \tag{40}$$

$$\begin{aligned}
c = &\pi^4d^2 + 4\pi^2\bar{g}^2q^2(1 + \pi^2 - 2\pi^2q + \pi^2q^2) + 4\pi^4d\bar{g}q(1-q) + \\
&+ \frac{4\pi^2\bar{g}^2}{(r_T+1)^2}(1 - 2q(r_T+1)).
\end{aligned} \tag{41}$$

A.2. Linear stability

The entries of the matrices in (31) are

$$\begin{aligned}
\frac{\partial t_{k+1}}{\partial t_k} &= \frac{r_B\dot{Z}_k - \bar{g}T_1 - f(t_k)T_1}{r_B\dot{Z}_k - \bar{g}T_1 - F_1(t_{k+1}) + F_1(t_k)}, \\
\frac{\partial t_{k+1}}{\partial \dot{Z}_k} &= \frac{-r_BT_1}{r_B\dot{Z}_k - \bar{g}T_1 - F_1(t_{k+1}) + F_1(t_k)}, \\
\frac{\partial \dot{Z}_{k+1}}{\partial t_k} &= \frac{\partial t_{k+1}}{\partial t_k}[f(t_{k+1}) + \bar{g}] - [f(t_k) + \bar{g}], \\
\frac{\partial \dot{Z}_{k+1}}{\partial \dot{Z}_k} &= -r_B + \frac{\partial t_{k+1}}{\partial \dot{Z}_k}[f(t_{k+1}) + \bar{g}],
\end{aligned} \tag{42}$$

$$\begin{aligned}
\frac{\partial t_{k+2}}{\partial t_{k+1}} &= \frac{r_T\dot{Z}_{k+1} - \bar{g}T_2 - f(t_{k+1})T_2}{r_T\dot{Z}_{k+1} - \bar{g}T_2 - F_1(t_{k+2}) + F_1(t_{k+1})}, \\
\frac{\partial t_{k+2}}{\partial \dot{Z}_{k+1}} &= \frac{-r_TT_2}{r_T\dot{Z}_{k+1} - \bar{g}T_2 - F_1(t_{k+2}) + F_1(t_{k+1})}, \\
\frac{\partial \dot{Z}_{k+2}}{\partial t_{k+1}} &= \frac{\partial t_{k+2}}{\partial t_{k+1}}[f(t_{k+2}) + \bar{g}] - [f(t_{k+1}) + \bar{g}], \\
\frac{\partial \dot{Z}_{k+2}}{\partial \dot{Z}_{k+1}} &= -r_T + \frac{\partial t_{k+2}}{\partial \dot{Z}_{k+1}}[f(t_{k+2}) + \bar{g}].
\end{aligned} \tag{43}$$

For period $T = 2$ motion the trace and determinant of the matrix DP in (31) are given by

$$\begin{aligned}
\mathrm{Tr}(DP) = &\frac{1}{\Theta_1\Theta_2}(r_B + r_BT_1[f(t_{k+1}) + \bar{g}])\cdot \\
&\cdot(r_T - r_TT_2[f(t_k) + \bar{g}]) - \frac{\Theta_3\Theta_4}{\Theta_1\Theta_2} - \\
&- \frac{r_TT_2}{\Theta_2}\left[f(t_k) + \bar{g} + \frac{\Theta_4}{\Theta_1}(f(t_{k+1}) + \bar{g})\right] + \\
&+ \frac{r_BT_1}{\Theta_1}\left[f(t_{k+1}) + \bar{g} - \frac{\Theta_3}{\Theta_2}(f(t_k) + \bar{g})\right],
\end{aligned} \tag{44}$$

$$\begin{aligned}
&\mathrm{Det}(DP) \\
&= \frac{r_B^2r_T^2\dot{Z}_k}{F_1(t_k) - F_1(t_{k+1}) + r_TF_1(t_k) - r_TF_1(t_{k+1}) + \bar{g}T_2 - \bar{g}r_TT_1 + \dot{Z}_kr_Br_T}
\end{aligned} \tag{45}$$

where $\Theta_1 = F_1(t_k) - F_1(t_{k+1}) + \dot{Z}_kr_B - \bar{g}T_1$, $\Theta_2 = F_1(t_k) - F_1(t_{k+1}) + \bar{g}T_2 + r_T\Theta_1$, $\Theta_3 = f(t_{k+1})T_2 + \bar{g}T_2 + r_T\Theta_1$ and $\Theta_4 = f(t_k)T_1 + \bar{g}T_1 + \dot{Z}_kr_B$.

References

[1] Yang Zhengbao, Zhou Shengxi, Zu Jean, Inman Daniel. High-performance piezoelectric energy harvesters and their applications. Joule 2018;2(4):642–97.
[2] Carneiro Pedro, Soares dos Santos Marco P, Rodrigues André, Ferreira Jorge AF, Simões José AO, et al. Electromagnetic energy harvesting using magnetic levitation architectures: A review. Appl Energy 2020;260:114191.
[3] Philippe Basset Dimitri Galayko. Electrostatic kinetic energy harvesting. Wiley; 2016.

[4] Thomson Gordon, Yurchenko Daniil, Val Dimitri V. Dielectric elastomers for energy harvesting. In: Energy harvesting. IntechOpen; 2018.

[5] Shao Jiajia, Willatzen Morten, Wang Zhong Lin. Theoretical modeling of triboelectric nanogenerators (TENGs). J Appl Phys 2020;128(11):111101.

[6] Zhao Huai, Ouyang Huajiang. A capsule-structured triboelectric energy harvester with stick-slip vibration and vibro-impact. Energy 2021;235:121393.

[7] Stephen NG. On energy harvesting from ambient vibration. J Sound Vib 2006;293(1–2):409–25.

[8] Hawes DH, Langley RS. Limits on the power available to harvest from broadband random excitation. J Sound Vib 2017;399:244–56.

[9] Bowen CR, Kim HA, Weaver PM, Dunn S. Piezoelectric and ferroelectric materials and structures for energy harvesting applications. Energy Environ Sci 2014;7:25–44.

[10] Salazar R, Larkin K, Abdelkefi A. Piezoelectric property degradation and cracking impacts on the lifetime performance of energy harvesters. Mech Syst Signal Process 2021;156:107697.

[11] Daqaq Mohammed F, Stabler Christopher, Qaroush Yousef, Seuaciuc-Osório Thiago. Investigation of power harvesting via parametric excitations. J Intell Mater Syst Struct 2009;20(5):545–57.

[12] Jia Yu, Yan Jize, Soga Kenichi, Seshia Ashwin A. Parametric resonance for vibration energy harvesting with design techniques to passively reduce the initiation threshold amplitude. Smart Mater Struct 2014;23(6):065011.

[13] Bobryk Roman V, Yurchenko Daniil. On enhancement of vibration-based energy harvesting by a random parametric excitation. J Sound Vib 2016;366:407–17.

[14] Bobryk RV, Yurchenko D. Enhancing energy harvesting by a linear stochastic oscillator. Probab Eng Mech 2016;43:1–4.

[15] Alevras Panagiotis, Theodossiades Stephanos, Rahnejat Homer. Broadband energy harvesting from parametric vibrations of a class of nonlinear Mathieu systems. Appl Phys Lett 2017;110(23):233901.

[16] Xia Guanghui, Fang Fei, Zhang Mingxiang, Wang Quan, Wang Jianguo. Performance analysis of parametrically and directly excited nonlinear piezoelectric energy harvester. Arch Appl Mech 2019.

[17] Nabholz Ulrike, Lamprecht Lukas, Mehner Jan E, Zimmermann André, Degenfeld-Schonburg Peter. Parametric amplification of broadband vibrational energy harvesters for energy-autonomous sensors enabled by field-induced striction. Mech Syst Signal Process 2020;139:106642.

[18] Dostal L, Pick MA. Theoretical and experimental study of a pendulum excited by random loads. European J Appl Math 2019;30(5):912–27.

[19] Yurchenko D, Alevras P. Parametric pendulum based wave energy converter. Mech Syst Signal Process 2018;99:504–15.

[20] Dotti Franco E, Sosa Mauricio D. Pendulum systems for harvesting vibration energy from railroad tracks and sleepers during the passage of a high-speed train: A feasibility evaluation. Theor Appl Mech Lett 2019;9(4):229–35.

[21] Huang Dongmei, Zhou Shengxi, Litak Grzegorz. Analytical analysis of the vibrational tristable energy harvester with a RL resonant circuit. Nonlinear Dynam 2019;97(1):663–77.

[22] Wang Junlei, Geng Linfeng, Zhou Shengxi, Zhang Zhien, Lai Zhihui, et al. Design, modeling and experiments of broadband tristable galloping piezoelectric energy harvester. Acta Mech Sin 2020.

[23] Fang Shitong, Zhou Shengxi, Yurchenko Daniil, Yang Tao, Liao Wei-Hsin. Multistability phenomenon in signal processing, energy harvesting, composite structures, and metamaterials: A review. Mech Syst Signal Process 2022;166:108419.

[24] Fu Hailing, Mei Xutao, Yurchenko Daniil, Zhou Stephanos, Nakano Kimihiko, et al. Rotational energy harvesting for self-powered sensing. Joule 2021. Accepted.

[25] Abdelkefi A. Aeroelastic energy harvesting: A review. Internat J Engrg Sci 2016;100:112–35.

[26] Wang Junlei, Geng Linfeng, Ding Lin, Zhu Hongjun, Yurchenko Daniil. The state-of-the-art review on energy harvesting from flow-induced vibrations. Appl Energy 2020;267:114902.

[27] Zhao Dan, Wang Xiaoman, Cheng Yuan, Liu Shaogang, Wu Yanhong, et al. Analysis of single-degree-of-freedom piezoelectric energy harvester with stopper by incremental harmonic balance method. Mater Res Express 2018;5(5):055502.

[28] Ai Rodrigo, Monteiro Luciana LS, Monteiro Paulo Cesar C, Pacheco Pedro MCL, Savi Marcelo A. Piezoelectric vibration-based energy harvesting enhancement exploiting nonsmoothness. Actuators 2019.

[29] Tien Meng-Hsuan, D'Souza Kiran. Method for controlling vibration by exploiting piecewise-linear nonlinearity in energy harvesters. Proc R Soc A: Math Phys Eng Sci 2020;476(2233):20190491.

[30] Yurchenko D, Lai ZH, Thomson G, Val DV, Bobryk RV. Parametric study of a novel vibro-impact energy harvesting system with dielectric elastomer. Appl Energy 2017;208:456–70.

[31] Todorov T, Valchev S, Moll F, Nikolov N, Nikolov R. Combined Piezoelectric vibroimpact energy harvester with improved performance. In: 2019 1st international conference on control systems, mathematical modelling, automation and energy efficiency. 2019. p. 650–655.

[32] Fu Yiqiang, Ouyang Huajiang, Davis R Benjamin. Triboelectric energy harvesting from the vibro-impact of three cantilevered beams. Mech Syst Signal Process 2019;121:509–31.

[33] Cao Dong-Xing, Xia Wei, Guo Xiang-Ying, Lai Siu-Kai. Modeling and experiment of vibro-impact vibration energy harvester based on a partial interlayer-separated piezoelectric beam. J Intell Mater Syst Struct 2020;1045389X20966057.

[34] Bernardo Mario, Budd Chris, Champneys Alan Richard, Kowalczyk Piotr. Piecewise-smooth dynamical systems. Springer-Verlag London; 2008.

[35] Ibrahim Raouf A. Vibro-impact dynamics: modeling, mapping and applications. Berlin, Heidelberg: Springer; 2009.

[36] Luo Albert CJ, Guo Yu. Vibro-impact dynamics. Oxford, UK: John Wiley & Sons Ltd; 2013.

[37] Shaw SW, Holmes PJ. A periodically forced piecewise linear oscillator. J Sound Vib 1983;90(1):129–55.

[38] Nordmark Arne B. Universal limit mapping in grazing bifurcations. Phys Rev E 1997;55(1):266–70.

[39] Chillingworth DRJ. Discontinuity geometry for an impact oscillator. Dyn Syst 2002;17(4):389–420.

[40] Luo Albert CJ. Period-doubling induced chaotic motion in the LR model of a horizontal impact oscillator. Chaos Solitons Fractals 2004;19(4):823–39.

[41] Wagg DJ, Bishop SR. Dynamics of a two degree of freedom vibro-impact system with multiple motion limiting constraints. Int J Bifurcation Chaos 2004;14(01):119–40.

[42] Wagg DJ. Periodic sticking motion in a two-degree-of-freedom impact oscillator. Int J Non-Linear Mech 2005;40(8):1076–87.

[43] Simpson DJW, Hogan SJ, Kuske R. Stochastic regular grazing bifurcations. SIAM J Appl Dyn Syst 2013;12(2):533–59.

[44] Kumar Pankaj, Narayanan S, Gupta Sayan. Stochastic bifurcations in a vibro-impact duffing–Van der pol oscillator. Nonlinear Dynam 2016;85(1):439–52.

[45] Bernardo Mario, Budd Chris, Champneys Alan Richard, Kowalczyk Piotr. Piecewise-smooth dynamical systems: theory and applications, Vol. 163. Springer Science & Business Media; 2008.

[46] Yan Y, Liu Y, Liao M. A comparative study of the vibro-impact capsule systems with one-sided and two-sided constraints. Nonlinear Dynam 2017;89:1063–87.

[47] Andreaus Ugo, De Angelis Maurizio. Nonlinear dynamic response of a base-excited SDOF oscillator with double-side unilateral constraints. Nonlinear Dynam 2016.

[48] Andreaus Ugo, Baragatti Paolo, De Angelis Maurizio, Perno Salvatore. A preliminary experimental study about two-sided impacting sdof oscillator under harmonic excitation. J Comput Nonlinear Dyn 2017.

[49] Andreaus Ugo, Baragatti Paolo, De Angelis Maurizio, Perno Salvatore. Shaking table tests and numerical investigation of two-sided damping constraint for end-stop impact protection. Nonlinear Dynam 2017.

[50] Andreaus Ugo, De Angelis Maurizio. Experimental and numerical dynamic response of a SDOF vibro-impact system with double gaps and bumpers under harmonic excitation. Int J Dyn Control 2019.

[51] Andreaus Ugo, De Angelis Maurizio. Influence of the characteristics of isolation and mitigation devices on the response of single-degree-of-freedom vibro-impact systems with two-sided bumpers and gaps via shaking table tests. Struct Control Health Monit 2020.

[52] Stefani Giulia, De Angelis Maurizio, Andreaus Ugo. Scenarios in the experimental response of a vibro-impact single-degree-of-freedom system and numerical simulations. Nonlinear Dynam 2021.

[53] Stefani Giulia, De Angelis Maurizio, Andreaus Ugo. Numerical study on the response scenarios in a vibro-impact single-degree-of-freedom oscillator with two unilateral dissipative and deformable constraints. Commun Nonlinear Sci Numer Simul 2021.

[54] Stefani Giulia, De Angelis Maurizio, Andreaus Ugo. Influence of the gap size on the response of a single-degree-of-freedom vibro-impact system with two-sided constraints: Experimental tests and numerical modeling. Int J Mech Sci 2021.

[55] Seifried R, Schiehlen W, Eberhard P. The role of the coefficient of restitution on impact problems in multi-body dynamics. Proc Instit Mech Eng Part K: J Multi-Body Dyn 2010;224(3):279–306.

[56] Durda Daniel D, Movshovitz Naor, Richardson Derek C, Asphaug Erik, Morgan Alexander M, et al. Experimental determination of the coefficient of restitution for meter-scale granite spheres. Icarus 2011;211:849–55.

[57] Gunkelmann Nina, Montaine Marina, Pöschel Thorsten. Experimental determination of the coefficient of restitution for meter-scale granite spheres. Phys Rev E Statist Nonlinear Soft Matter Phys 2014;89:1550–2376.

[58] Flores Paulo, Lankarani Hamid M. Dissipative contact force models. In: Contact force models for multibody dynamics. Springer International Publishing; 2016, p. 27–52.

[59] Lai ZH, Wang JL, Zhang CL, Zhang GQ, Yurchenko D. Harvest wind energy from a vibro-impact DEG embedded into a bluff body. Energy Convers Manage 2019;199:111993.

[60] Qian Jiamin, Chen Lincong. Random vibration of SDOF vibro-impact oscillators with restitution factor related to velocity under wide-band noise excitations. Mech Syst Signal Process 2021;147:107082.

[61] Mehnert Markus, Hossain Mokarram, Steinmann Paul. A complete thermo–electro–viscoelastic characterization of dielectric elastomers, part I: Experimental investigations. J Mech Phys Solids 2021;157:104603.
[62] Serdukova Larissa, Kuske Rachel, Yurchenko Daniil. Stability and bifurcation analysis of the period-T motion of a vibroimpact energy harvester. Nonlinear Dynam 2019;98(3):1807–19.
[63] Serdukova Larissa, Kuske Rachel, Yurchenko Daniil. Post-grazing dynamics of a vibro-impacting energy generator. J Sound Vib 2021;492(3):115811.
[64] Xu Zewang, Zheng Shaodi, Wu Xiaotian, Liu Zhengying, Bao Ruiying, et al. High actuated performance MWCNT/Ecoflex dielectric elastomer actuators based on layer-by-layer structure. Composites A 2019;(125).
[65] Serdukova Larissa, Kuske Rachel, Yurchenko Daniil. Analyzing the competition between grazing and period-doubling bifurcations in a vibro-impacting energy generator. 2021, (in preparation).